Icarus 410 (2024) 115722

Contents lists available at ScienceDirect

Icarus

journal homepage: www.elsevier.com/locate/icarus

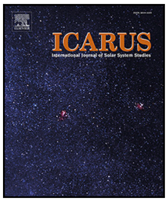

Research Paper

LineaMapper: A deep learning-powered tool for mapping linear surface features on Europa

Caroline Haslebacher [a,*], Nicolas Thomas [a], Valentin T. Bickel [b]

[a] *University of Bern, Physikalisches Institut, Sidlerstrasse 5, 3012 Bern, Switzerland*
[b] *University of Bern, Center for Space and Habitability, Gesellschaftsstrasse 6, 3012 Bern, Switzerland*

ARTICLE INFO

Dataset link: LineaMapper: a deep learning-powered tool for mapping linear surface features on Europa (Haslebacher et al., Icarus, 2023) accompanying data (Original data)

Keywords:
Satellites
Surfaces
Europa
Geological processes
Image processing

ABSTRACT

As discontinuities of the smooth icy surface, linear surface features might be directly or indirectly linked to Europa's subsurface ocean. Mapping and categorising Europa's lineaments is a means of retrieving information that could be linked to their formation history. As of today, planetary mapping is mainly conducted manually, which is tedious and subject to human bias once data sets become large. Mapping is further complicated by the heterogeneous quality and coverage of the available image data.

Here, we train LineaMapper, a convolutional neural network (Mask R-CNN), to conduct instance segmentation of the four main units of linear surface features on Europa: bands, double ridges, ridge complexes and undifferentiated lineae. LineaMapper is trained on the basis of 15 mosaics from the Galileo solid-state imager data, yielding 930 training tiles. With LineaMapper, we provide a new method that facilitates detailed mapping of lineaments in Galileo images. LineaMapper could be applied to data to be returned by the Europa Imaging System (EIS) onboard the Europa Clipper mission. We validate LineaMapper v1.0 on an independent test set. On this test set, LineaMapper shows an overall higher precision than recall. In other words, there are more non-detections of actual lineaments than there are false detections of lineaments. The model shows the most correct predictions for double ridges (highest precision), while the most complete detections happen for ridge complexes (highest recall), compared with the ground truth. In some cases, LineaMapper preserves the cross-cutting relationships. The biggest strength of LineaMapper lies in its speed and tunable output. In the future, LineaMapper can be retrained, fine tuned and applied to similar looking features, for example wrinkle ridges on Venus, ridges on other planets and moons or even dust devil tracks on Mars.

1. Introduction

The surface of Jupiter's icy moon Europa shows curvilinear geological features called lineaments. Some of the lineaments on Europa span over a hemisphere, while others appear only at regional scales (Prockter and Patterson, 2009). These curvilinear surface features that potentially stem from cracks in the ice shell (e.g. Harada and Kurita, 2006; Geissler et al., 1998a,b) are of keen interest because they might provide direct or indirect connections (e.g. Greenberg et al., 1998a; Pappalardo et al., 1999; Greenberg and Geissler, 2002; Rhoden et al., 2015; Kalousová et al., 2016; Dameron and Burr, 2018) to Europa's subsurface ocean, allowing a remote sensing study of the surface material originating from the subsurface ocean.

The solid-state imager (SSI) onboard the Galileo mission (Belton et al., 1992) observed Europa with eight band pass filters from near ultra-violet to near infrared. Between 1996 and 2002 during 11 flybys, SSI collected 700 individual 800 × 800 px images, resulting in a data set of almost 2 gigabyte. The Galileo SSI data set has a wide range of resolutions, from 6 m/px up to 20 km/px. Two regional mosaics were acquired in Encounters 15 and 17, one covers a 250 km wide area of the trailing hemisphere from north to south and the other the same on the leading hemisphere.

Based on a global map mosaiced from Galileo and Voyager images at a scale of 1:15M (U.S. Geological Survey, 2002), Leonard et al. (2019) mapped the whole surface of Europa into several distinct surface feature units such as chaos, bands, impact crater units and linear features. Their mapping shows that ridged plains make up most of the surface area. Ridged plains appear as seemingly smooth terrain that contains a high number of undifferentiated lineae if observed at higher resolution.

The SSI images composing the two regional mosaics with a resolution of about 230 m/px cover approximately 10% of Europa's surface (Doggett et al., 2009). At this regional scale, different categories

---

* Corresponding author.
E-mail addresses: caroline.haslebacher@unibe.ch (C. Haslebacher), nicolas.thomas@unibe.ch (N. Thomas), valentin.bickel@unibe.ch (V.T. Bickel).

https://doi.org/10.1016/j.icarus.2023.115722
Received 2 March 2023; Received in revised form 21 June 2023; Accepted 25 July 2023

of lineaments were identified, with the double ridge as the most common identifiable linear surface feature (Prockter and Patterson, 2009). Although many formation hypotheses exist for double ridges (Sullivan et al., 1998; Aydin, 2006; Gaidos and Nimmo, 2000; Nimmo and Gaidos, 2002; Han and Showman, 2008; Head et al., 1999; Greenberg et al., 1998b; Pappalardo and Coon, 1996; Tufts et al., 2000; Melosh and Turtle, 2004; Han and Melosh, 2010; Turtle et al., 1998; Crawford and Stevenson, 1988; Kadel et al., 1998; Dombard et al., 2013; Craft et al., 2016; Johnston and Montési, 2014; Culberg et al., 2022), observations do not provide conclusive evidence for one specific hypothesis. Also for a bundle of parallel-going, anastomosing and intertwining double ridges, called a ridge complex, no formation hypothesis (Geissler et al., 1998b; Greenberg et al., 1998b; Figueredo and Greeley, 2000; Manga and Sinton, 2004; Aydin, 2006) is predominantly accepted. At the time of writing, the community largely agrees on the formation mechanism for cycloids and subtypes of bands. Cycloids are curvilinear features consisting of arcuate segments interrupted by cusps (Hoppa et al., 1999). They form in one orbit around Jupiter due to diurnal stresses that arise from Europa's slightly eccentric orbit, although other stress contributors, such as non-synchronous rotation and obliquity, might play a role (Hoppa et al., 1999; Hurford et al., 2007, 2009; Pappalardo et al., 2016; Marshall and Kattenhorn, 2005; Rhoden et al., 2010; Groenleer and Kattenhorn, 2008; Poinelli et al., 2019; Rhoden et al., 2021). Bands are another tectonically important category of Europan linear surface features. There exist several different subunits of bands. A common subunit is the dilational band, which is a zone of divergence that can be clearly identified with the help of adjacent features (Tufts et al., 2000; Prockter and Patterson, 2009).

Selected images of the Galileo and Voyager data set have been mapped on a regional scale (Greenberg et al., 1999; Greeley et al., 2000; Figueredo and Greeley, 2000, 2004; Kattenhorn, 2002; Sarid et al., 2004, 2005, 2006; Patterson et al., 2006; Collins et al., 2022; Leonard et al., 2018; Noviello et al., 2019; Bradák et al., 2023). However, exhaustive detailed mapping is a time consuming process, because features sometimes do not have clear borders and the classification of units is not straightforward. Even so, the Galileo SSI dataset is small enough to map all identifiable features manually. Mainly because of the inhomogeneous and sometimes low resolution of Galileo SSI data, no detailed global mapping of linear surface features has been provided yet. Such a map could be used to extract morphological parameters on a global scale. Bradák et al. (2023), for example, manually segmented lineaments in the region of Rhadamanthys Linea at a resolution of 228 m/px. Their analysis suggests three different generations of lineament formation and calls for a global analysis of lineaments at this scale. Rhoden and Hurford (2013) analysed azimuths of 75 lineaments that provide evidence that spin pole precession connected to an obliquity of approximately 1 ° is the dominant stress that creates the wide distribution of lineament azimuths. Their study focused on an area of only 36 × 61 km^2 in the Bright Plains region, which equals less than 0.01% of the total surface area of Europa, and would benefit from a larger study area. However, a detailed global analysis at the regional scale will only be possible with the global dataset returned by Europa Clipper in the 2030's.

The Europa Imaging System (EIS, Turtle et al., 2023) onboard the Europa Clipper mission is expected to downlink a volume of approximately 1-2 Tb in the 2030's, which is 60–125 times greater than the Galileo data set. The EIS narrow angle camera (NAC) and wide angle camera (WAC) will cover more than 80% of the surface with a resolution better than 100 m/px. An automated mapping tool on the basis of deep learning could provide a more efficient mapping of this data set. The quality of these mappings could be assessed with an EIS test set, manually mapped by a scientist.

Deep learning is a subdivision of machine learning, which itself is embedded under the umbrella of artificial intelligence. After increased computing powers and possibilities to store data in big amounts became available around 2012, deep learning activities started to deliver powerful algorithms (e.g. Wang and Raj, 2017; Goodfellow et al., 2016). Computer vision tasks such as image classification, object detection, semantic segmentation and instance segmentation, for which a solution has long been sought (Gonzalez and Wintz, 1977), began to be solved with increased performance by deep learning networks. In planetary sciences, deep learning models are now on the rise, even though lagging behind other space-related fields, for example heliophysics (Azari et al., 2020). In the field of remote sensing, where more and more data volume can be acquired in future missions, deep learning is used more and more for a variety of applications. Barrett et al. (2022) train the "Novelty or Anomaly Hunter – HiRISE" NOAH-H for pixel-wise mapping into different terrain classes such as a variety of bedrock terrain or boulder fields. Bickel et al. (2019) trained a convolutional neural network (CNN), the RetinaNet, for automated lunar rockfall detection and classification, and later Bickel et al. (2020a) applied it to the Moon on a global scale. Bickel et al. (2020b) re-trained their network for rockfall detection on Mars. There have also been attempts to extract features with curvilinear shapes using deep learning. Aghaee et al. (2021) trained a CNN for semi-automated lineament detection in remote sensing data for the exploration of minerals on Earth. General instance segmentation of sophisticated object shapes, including intersecting linear features, was explored by, for example, Mais et al. (2020).

Recently, He et al. (2018) introduced the Mask R-CNN, a region-based convolutional neural network, for object instance segmentation, by extending the Faster R-CNN with a masking branch. This network was bench-marked on the Common Objects in COntext (COCO) test set, which contains 80 different object classes. In remote sensing, the Mask R-CNN framework is used for a variety of applications: the detection of ships and airplanes on Earth (Gan et al., 2020), automated segmentation of ice-wedged polygons in the Arctic tundra on Earth (Zhang et al., 2020) and automated spacecraft navigation using automatically detected craters as landmarks (Del Prete and Renga, 2022). Closest to our application is the recent publication by Nixon et al. (2023), where a Mask R-CNN is trained for the detection of ice blocks in chaos terrain on Europa.

To facilitate mapping of linear surface features in general and specifically on Europa, we provide, for the first time, a Mask R-CNN model that can detect, classify and map linear surface features. We call our Mask R-CNN model *LineaMapper* Version 1.0 LineaMapper can ultimately help geologists to map linear surface features on Europa in less time, with a high precision and a deterministic method. It is currently trained on a subset of the Galileo data and takes into account four different categories of linear surface features: (1) bands (2) double ridges (3) ridge complexes and (4) undifferentiated lineae.

2. Methods

2.1. Lineament categories

Mainly following Prockter and Patterson (2009), we characterise bands, double ridges, ridge complexes, and undifferentiated lineae contained in ridged plains, in the following subsections. Examples are given in Fig. 1.

Bands

A band is defined as a tabular zone with a uniform albedo. It can contain subparallel ridges (lineated band) or smooth terrain (smooth band). Bands exhibit a clear boundary to the adjacent terrain, which is consistent alongside the band. As zones of convergence or spreading, bands are linked directly to the motion of plates, which occurs episodically at a regional scale (Kattenhorn and Prockter, 2014; Collins et al., 2022). If the features at the margins of the bands fit together when the band is removed, the band can be classified as a dilational (pull-apart) band, which is a zone of spreading. Bands are in general the widest

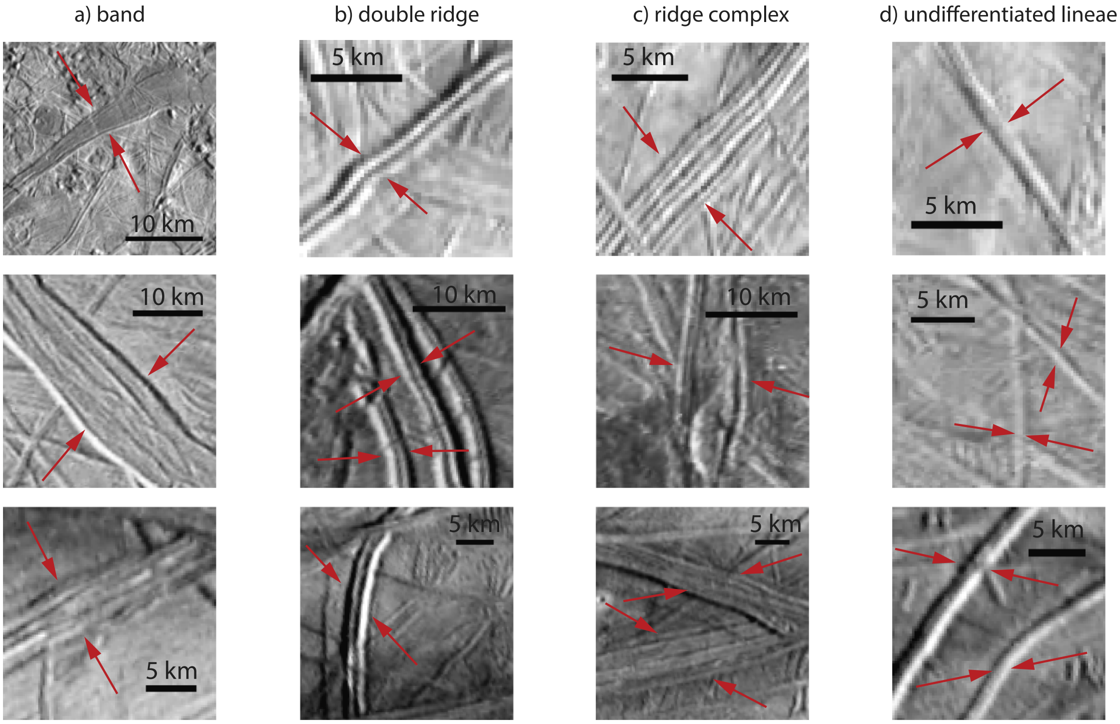

Fig. 1. Units. Examples of the four investigated units: (a) bands, (b) double ridges, (c) ridge complexes, and (d) undifferentiated lineae. The examples in the first row are from observation '11ESREGMAP01EXCERPT1', examples in the second row are from observation '25ESDARKBP01' and examples in the third row are from observation '15ESREGMAP01EXCERPT1'. The arrows indicate the borders of the units.
Source: Figure created with data from Bland et al. (2021).

linear surface features. Therefore, we include a width constraint in the mapping guideline (Fig. A.14) which comes into play if no tabular zone with clear boundaries can unquestioningly be defined. In this case, features of question that are wider than 15 km are mapped as bands (Figueredo and Greeley, 2000). Prominent bands are Agenor Linea (convergence band) and Thynia Linea (dilational band). The examples in Fig. 1 show that a band can be hard to distinguish from a ridge complex due to the ridged terrain inside ridged bands. The colour we use for bands is purple (hex: #7F4A9D) and was taken from Leonard et al. (2019).

Double ridges

A double ridge consists of two ridge crests flanking an axial trough (Greenberg et al., 1998a; Kattenhorn and Hurford, 2009). Double ridges are the most common features (Prockter and Patterson, 2009). Interestingly, double ridges were formed throughout Europa's surface history: double ridges appear in the old ridged plains as well as as very young features implied by very few cross-cuttings (Kattenhorn and Hurford, 2009). Uniform morphological characteristics are found along double ridges and they can be extremely straight, while varying in length between tens to hundreds of kilometres (e.g. Greeley et al., 2000). The examples in Fig. 1.b show that a double ridge is clearly identifiable with its axial trough, and also in noisy images such as in the first row of Fig. 1.b. If no axial trough can be clearly identified (e.g. Fig. 1.d, last row), the feature is labelled as an undifferentiated lineae. The colour we use for double ridges is dark orange (hex: #ED9A22) and was taken from Leonard et al. (2018).

Ridge complexes

Double ridges that are overlapping, anastomosing, inosculating, and follow a unified direction are called ridge complexes. The margins of a ridge complex are identifiable, while they can be sinuous and individual ridges may join or divert from a ridge complex, and might exhibit a dark[1] deposit alongside the ridge complex (Lucchitta and Soderblom, 1982). It is possible that, due to a created weakness, the formation of several double ridges is triggered by one fracture (Greenberg et al., 1998a; Geissler et al., 1998b; Figueredo and Greeley, 2000; Manga and Sinton, 2004). Other possible formation theories describe volumetric deformation (Aydin, 2006) and the formation in an isotropic and tensile stress field (Patterson and Head, 2010). Wide and long ridge complexes are observable on a global scale with prominent examples being Agave Linea, Belus Linea and Ephemeus Linea (Patterson and Head, 2010). Fig. 1.c shows four identified ridge complexes. The colour we use for ridge complexes is light orange (hex: #FFD380) and was taken from Leonard et al. (2018).

Undifferentiated lineae

Undifferentiated lineae are linear surface features identifiable by lower or higher albedo than the surroundings that cannot be distinguished further (Leonard et al., 2019). Some undifferentiated lineae reveal themselves as an identifiable lineament category at a higher resolution. Ridged plains contain mainly undifferentiated lineae that are overprinted by younger features. The term 'ridged plains' for old background terrain that is filled with a high number of short, often uncrossed undifferentiated lineae, was introduced for Europa by Geissler et al. (1998b), Greeley et al. (1998), Head et al. (1998) and Figueredo and Greeley (2000). The example of an undifferentiated linea in Fig. 1.d, third row, on the left in the tile, contains a hint that at a higher resolution, this instance might turn out to be a double ridge. The colour we use for undifferentiated lineae is pale pink (hex: #D9B6D6) following Leonard et al. (2019).

---

[1] At visible wavelengths.

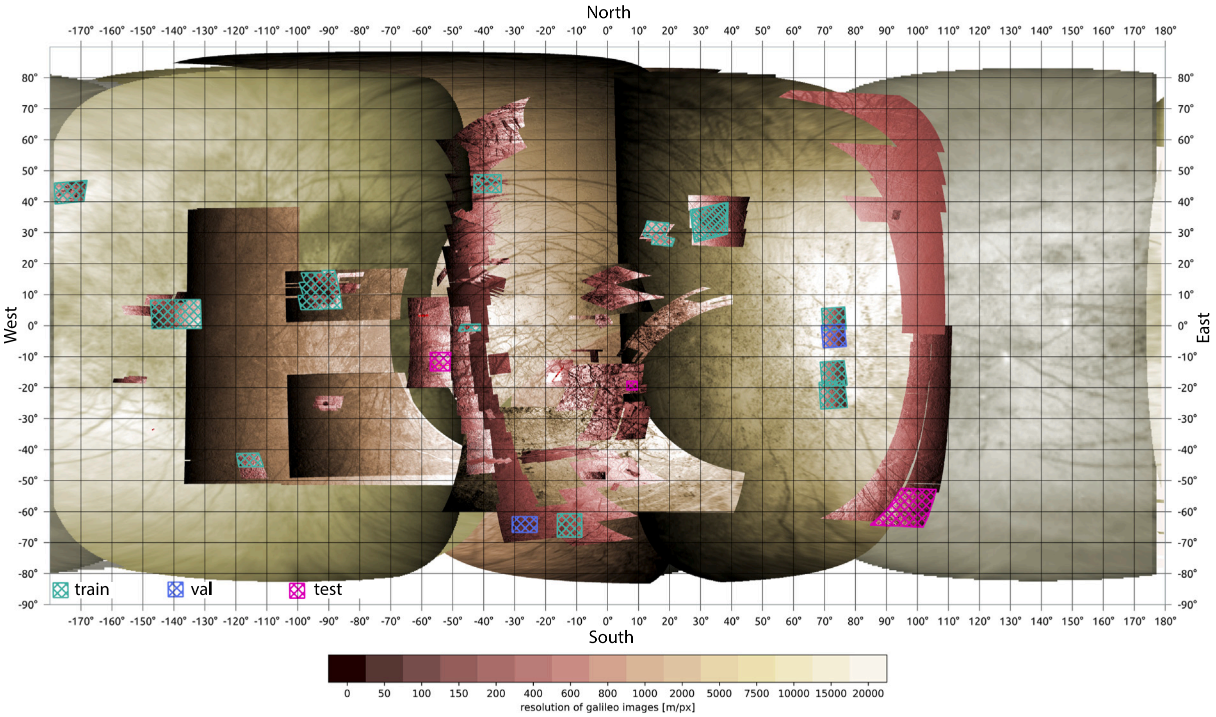

Fig. 2. Map. A Galileo SSI map based on data from Bland et al. (2021) in equirectangular projection showing the locations of the training, validation, and test mosaics. The map is colour coded by resolution in meters per pixel. The observation areas mapped for training LineaMapper are depicted in green, for validation in blue, and for testing in pink. Map created using the Free and Open Source QGIS. (For interpretation of the references to colour in this figure legend, the reader is referred to the web version of this article.)

2.2. *Manual segmentation of selected images*

We trained LineaMapper in a supervised manner, which means that we let the network learn by comparing its output to a solution, called "ground truth". To create this ground truth, in our case the mapped lineaments, we manually segmented lineaments in selected Galileo images. This selection is shown in Table 1, Fig. 2 and in more detail in the appendices (Figs. B.15 and B.16), and is explained in detail below.

We imported photogrammetrically corrected mosaics and individual observations released by Bland et al. (2021) into QGIS version 3.22 (QGIS Development Team, 2022). We selected images with a horizontal pixel resolution between 150 and 600 m/px. This is the resolution range where most Galileo images were acquired. Our selection assures that different illumination conditions and regions are represented to train the network with a diverse data set.

Each lineament was mapped as a polygon. Fig. 1 shows that identifying features and their borders is not always straight-forward. Therefore, we followed our guideline (Fig. A.14) dedicated to map lineaments as consistently as possible. The guideline tests first if the lineament is longer than 30 px, wider than 4 px and has a contrast higher than 0.08 when evaluating the calibrated I/F (intensity divided by solar flux). A contrast in I/F of 0.08, resulting from changes in brightness, can be expected from the topography associated with the features, if the features are illuminated not exactly parallel to their azimuth and if the topography is distorted remarkably. At the same time, a contrast limit introduces a known bias neglecting features illuminated directly parallel to their azimuth. Finally, following the guideline, which transforms the definitions described in Section 2.1 into a decision tree (Fig. A.14), the lineament can be categorised.

The manual segmentation was done by a single person, who went through each image twice. Because detailed mapping of all resolvable linear surface features in Galileo images is a challenging task, the mapping conducted by this person may be flawed and influenced by individual human biases. Therefore, what we mean when we use the term 'ground truth' would be better reflected by the term 'human mapping', which we will use in the following when we want to make this distinction clear.

2.3. *Deep learning framework*

2.3.1. *Justification for a deep learning framework*

Firstly, mapping of lineaments is a time-expensive process, since for each lineament, a polygon must be drawn around it by selecting boundary points. For example, the person mapping for this study needed 4 h of focused time for mapping all 260 features in observation '17ESREGMAP03'. On average, this amounts to 1 min per feature. Observation '17ESREGMAP03' covers less than 0.1% of the Europan surface with a resolution of 234 m/px in equirectangular projection. If we assume the same density of lineaments, mapping the whole surface at that speed and resolution would take 4000 h, equal to 500 days of 8-hour work-days.

Secondly, no classical line-detection algorithm is suitable for instance segmentation. Algorithms such as the Hough transform (Duda and Hart, 1972), the probabilistic Hough transform (Kiryati et al., 1991), the Radon transform (Radon, 1917) and algorithms in the Fourier frequency domain (e.g. Ruzicka et al., 2021) are valuable techniques for line detection. However, they are hard to tune and not easily generalisable to small changes in the image, such as different incidence angles. Furthermore, these algorithms output parameters describing the detected straight lines. Out of these, it is not straightforward to compose a mask, which covers all pixels that belong to one instance of a lineament. For straight instances of undifferentiated lineae and double ridges, these algorithm might eventually work, but not for bands and ridge complexes, which are not well described by single lines. Also for curved instances of lineaments, these algorithms are impractical. Due to the aforementioned reasons, deep learning based instance segmentation provides the best method available as of today.

Table 1
Overview of manually segmented Galileo observations. The segmentations were done directly on the mosaics from Bland et al. (2021) indicated in column 'Observation ID'. The observing geometries (incidence angle, phase angle, etc.) were extracted from the individual Galileo observations displayed in column 'Clock ID'. If there are several individual observations belonging to one segmented mosaic or mosaic excerpt, the geometries are given for the observation with a bold clock ID.

Data set	Observation ID	Clock ID	incidence angle [°]	phase angle [°]	emission angle [°]	north azimuth [°]	Horizontal pixel scale [m/px]	vertical pixel scale [m/px]	Filter
Training set	G7ESLOWFOT01	C0389768826R, C0389767113R, **C0389767100R**, C0389767126R	35.799	5.024	37.75	84.08	456.955	548.245	Green
	G7ESTYRMAC01	**C0389772500R**, C0389772507R	47.131	15.696	38.293	285.068	671.686	691.257	Green
	G7ESTYRMAC02	C0389773000R	47.327	18.661	37.156	280.565	623.652	678.529	IR-9680
	G7ESAPEXCR01	C0389778842R	79.882	62.558	17.331	274.27	513.3	490.1	Clear
	G7ESAPEXCR04	C0389780135R	80.963	72.834	20.446	273.756	521.692	549.536	Clear
	G7ESAPEXCR05	C0389780563R	81.424	75.995	26.535	273.862	532.25	593.695	Clear
	E4ESMACSTR01	C0374667300R	80.854	54.82	26.471	90.437	701.49	634.179	Clear
	E6ESDRKLIN01	**C0426267401/00R**, C0426267513R, C0426267427/26R, C0426267452R, C0426267478R, C0426267366/65R	59.391	95.183	36.872	91.774	213.2	174.2	Green
		C0383713713R, C0383713701R, C0383713700R, C0383713726R, C0383713739R, C0383713752R, C0383713765R	82.336	39.217	45.345	93.386	249.417	194.51	Clear
	11ESCOLORS01–01	**C0420617239R**, C0420617213R, C0420617226R, C0420617200R	66.649	61.216	5.434	91.129	289.9	288.8	IR-9680
	12ESFRTPLT01EXCERPT1	C0426267200/01R	85.346	93.08	52.224	91.342	185.3	294.8	Clear
	15ESREGMAP01EXCERPT1	**C0449961914R**, C0449961839R	73.942	63.463	45.393	93.747	230.173	327.339	Clear
	17ESREGMAP03	C0466677052R	82.985	92.198	56.516	268.765	243.769	420.854	Clear
	25ESDARKBP01	C0527275700R	64.94	33.593	33.003	287.91	249.43	234.4	Clear
Validation set	G7ESAPEXCR02	**C0389779270R**, C0389779271R	80.167	66.098	15.347	274.115	511.713	501.176	Clear
	17ESREGMAP01EXCERPT2	C0466664352R	78.969	71.61	56.425	95.438	226	408	Clear
Test set	17ESREGMAP01EXCERPT1	C0466664366R	73.835	72.019	59.544	94.497	232	442	Clear
	11ESREGMAP01EXCERPT1	C0420619278R	80.963	72.834	20.446	89.254	227.638	228.951	Clear
	14ESWEDGES01EXCERPT1	C0440955239R	55.549	74.323	34.093	269.757	352.8	262.5	Clear

2.3.2. *Architecture and hyperparameters*

The architecture of a network defines the structure into which the trained model fits. An architecture uses a selection of set parameters, such as the number of layers or the number of input channels of the input image. On the contrary, the term 'hyperparameter' is used for modifiable parameters (the weights that are saved as the output of the training still fit into the architecture, no matter the combination of hyperparameters), such as the learning rate (how fast the network learns by adjusting its weights) or the batch size (how many images are shown to the network at the same time). We choose the Mask R-CNN (He et al., 2018) architecture as a well-tested general instance segmentation framework. In 2018, the Mask R-CNN outperformed the winners of the COCO 2016 challenge in instance segmentation. It achieved an average precision (explained in Section 2.3.5) of 37.1% averaged over Intersection over Union (IoU; explained in Section 2.3.5) thresholds of 0.5 to 0.95 with a ResNeXt-101-FPN backbone.

The Mask R-CNN scheme and the whole workflow of LineaMapper are visualised in Fig. 3. LineaMapper outputs for each predicted bounding box (a rectangle that encompasses the detected lineament) (1) a probability score, which indicates how certain the network is about its detection, (2) a label, which tells us the predicted class (= geological unit), and (3) a mask, which is a binary image providing the lineament segmentation: the pixels (inside the bounding box) that belong to the detected lineament are set to 1, the rest to 0.

For LineaMapper, we used a ResNet-50 (He et al., 2016) as the backbone with weights pretrained on 3-channel (RGB) ImageNet (Deng et al., 2009) data. Although we found only a marginal difference between pretrained weights and initialised weights, we decided to use pretrained weights for increased robustness. Additionally, we chose 3-channel RGB input to allow for colour data in light of Europa Clipper EIS colour data. We fine tuned the Mask R-CNN with 3 trainable backbone layer blocks (5 would be the maximum; in our case, 2 layer blocks were frozen) to allow the weights to adopt significantly to linear features in Galileo images. We used a stochastic-gradient descent (SGD) optimiser (Robbins and Monro, 1951), a standard, well-used and tested optimiser at the time of writing. An optimiser helps to decrease the initial learning rate in a way that accelerates convergence of a network. Through trial-and-error to find the optimum, the learning rate was set to 0.01 and the batch size to 6 images. The minimum and maximum size that the input tile was resized to was 200 × 200 and 300 × 300 pixel.

2.3.3. *Hardware and software*

The model was trained on a Predator Orion 5000 with an Nvidia Geforce RTX 3080 GPU (10 GB GDDR6X dedicated memory, 8704 CUDA cores, 760 GB/s memory bandwidth, CUDA driver 11.6.134), Intel Core i9-10900K CPU (10 cores, 20 threads, 3.70 GHz) on a Windows 10 Enterprise operating system. We used the *pytorch* (Paszke et al., 2019) python library version 1.11.0 implementation of the Mask R-CNN. Additionally, we used the python library *torchvision* (Marcel and Rodriguez, 2010) version 0.12.0 for training and inference.

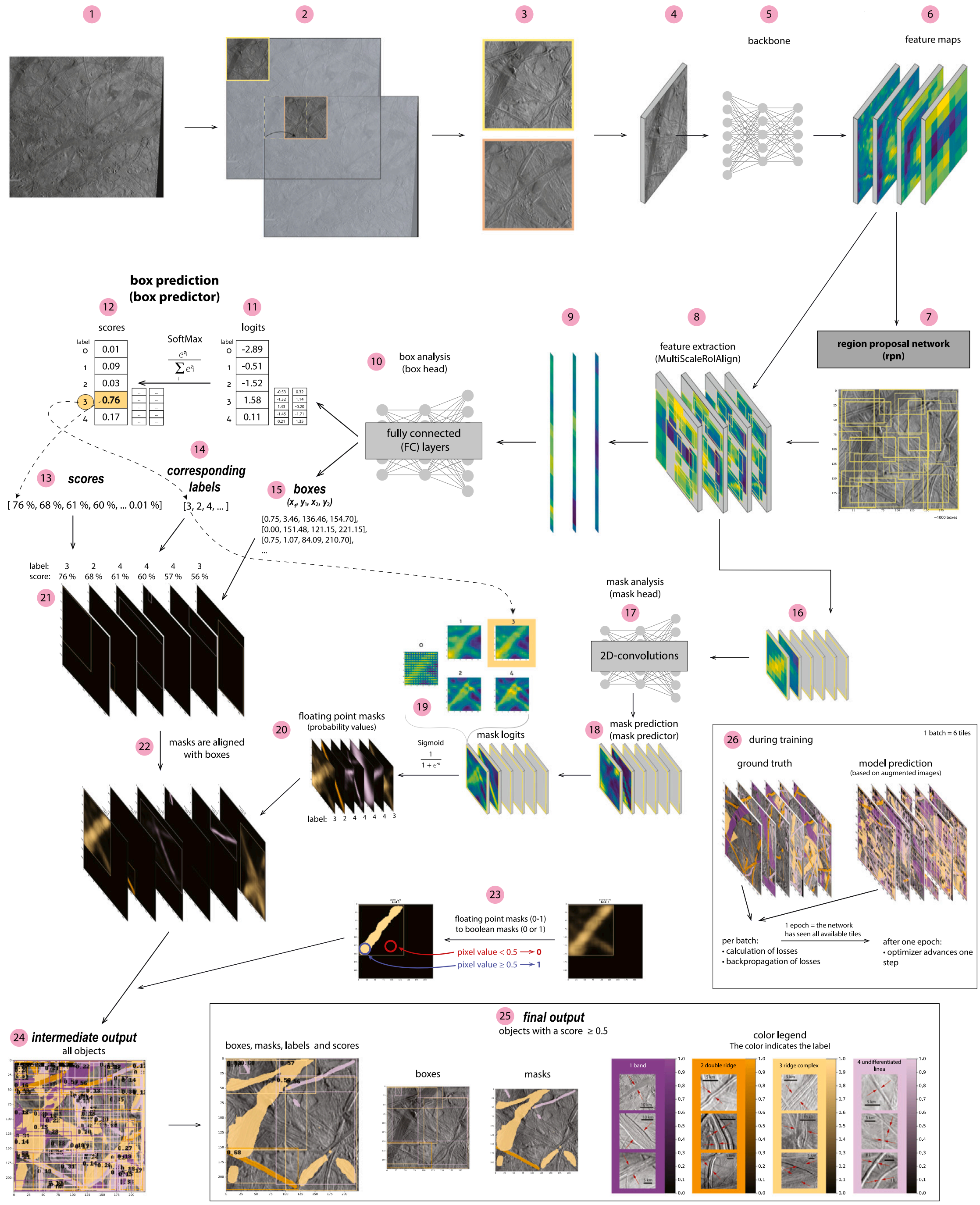

Fig. 3. Visualisation of the workflow with LineaMapper from image insertion to output. An input black-and-white image (1) is tiled up with a moving window tiling algorithm in (2). The tiling window algorithm moves by half the tile size of the input image, in our case by 112 pixels, to get partially overlapping tiles (3). We follow the path of one such black-and-white tile, which is converted into a 3-channel array by repeating the black-and-white channel three times to imitate an RGB input, and which is normalised (mean: [0.485, 0.456, 0.406], standard deviation: [0.229, 0.224, 0.225]) in step (4). This array is fed into the backbone of the Mask R-CNN (5), for which we chose a ResNet-50-FPN, which is 50 layers deep and outputs a feature pyramid network (FPN). The task of the backbone is to extract features based on which the Mask R-CNN makes predictions. The output of the backbone network is a pyramid of four 256-channel feature maps (6). The feature maps are the basis for the region proposal network (7), which proposes bounding boxes that potentially contain objects. The proposals, or region of interests (RoI) are aligned (8). The box prediction (9–15) is separated from the mask prediction branch (16–20). For the box branch, the RoIs are flattened (9) and then fed into a fully connected network (10). This box head outputs an array of size (N,4) for the bounding boxes (15) and an array of size (N, nclasses) containing the logit values (11) (logit of probability = logarithm of the odds), with N being the number of proposals. The logits (11) are converted to probability scores (values between 0 and 1) with a SoftMax function, which essentially normalises the logits values. The highest probability score in (12) defines the label of a detection. This is done for each box proposal and leads to the output of the box predictor (21): scores (13), labels (14) and boxes (15). The mask head uses the extracted masks reshaped to squares (16) as an input. It outputs refined predictions in 256-channels (18), which are turned into segmentation mask logits channels by the mask predictor (18). The arrays in (19) are 28 × 28 px, nclasses-channel images. For the output of the floating point masks (20), it only takes the image with the correct label from (14). The floating point 28 × 28 pixel masks are finally combined and pasted into the boxes (22). A non-maximum suppression algorithm now filters duplicates, and the top-scoring, maximum 100 detections are passed on. Finally, the floating point masks are converted to boolean (binary) masks by simple thresholding (23). This leaves us with a maximum of 100 detected objects (24). As the last step, we choose a score threshold to display the most confident detections only (25). The final output (25) consists of objects with boxes, masks, labels and scores. The box can be bigger than the mask due to the thresholding step in (23). During training (26), the model predictions are compared to the ground truth, from which the losses (e.g. cross-entropy binary loss function for the mask loss) are calculated. This happens per batch (=6 tiles). The losses are backpropagated through the network to improve it. Once the network has seen all available tiles (we call this one epoch), the optimiser (here: Adam optimiser) advances one step. Note that class 0 is an ‘empty’ class.

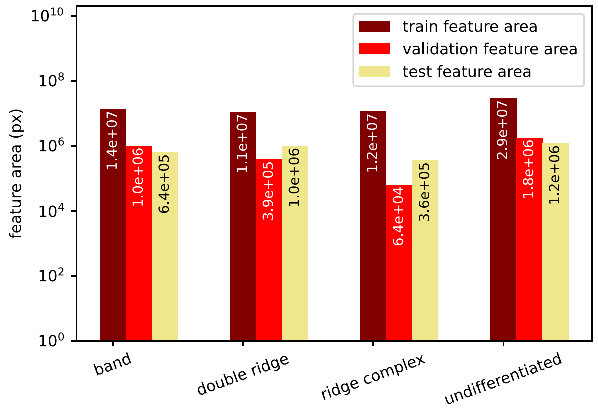

Fig. 4. Area of bounding boxes in the training, validation and test set tiles.

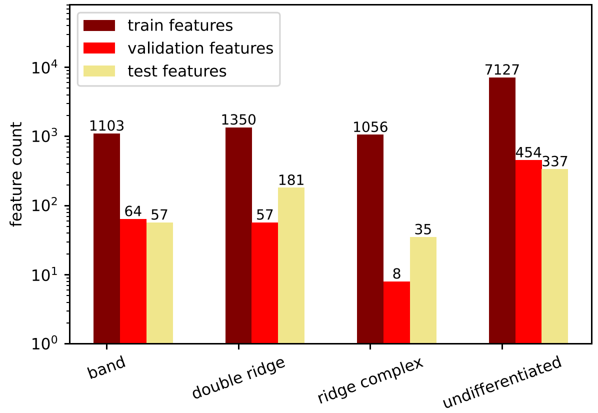

Fig. 5. Feature count of instances in the training, validation and test set tiles.

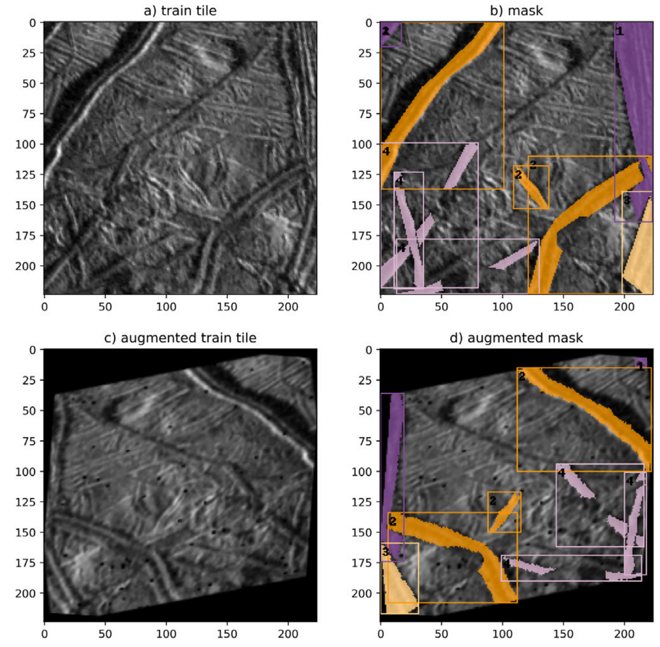

Fig. 6. Augmentation. One example of an augmented training tile. Bands (1) are shown in purple, double ridges (2) in dark orange, ridge complexes (3) in light orange and undifferentiated lineae (4) in pale pink. (For interpretation of the references to colour in this figure legend, the reader is referred to the web version of this article.)

2.3.4. *Training LineaMapper*

It is out of the scope of this work to go into detail about how exactly the model learns. Readers are deferred to Goodfellow et al. (2016) for an introduction to Deep Learning. Nevertheless, the sketch in Fig. 3, especially step (26), should help to get an idea. In this section, we go into detail about the training, validation and test data set. We used a tiling window algorithm to divide the mapped Galileo images into smaller tiles of size 224 × 224 px. The tiling window algorithm moves by half the tile size of the input image, in our case by 112 pixels, to get partially overlapping tiles (Fig. 3, step 2 and 3). Trial-and-error experiments to find the optimal tile size were conducted (not shown). Since linear surface features on Europa often span more than a 224 × 224 pixel area, the network might perform slightly better on tiled-up lineaments, which appear in adjacently windowed tiles, than on an independent surface area. Therefore, we ensure that the model performance results are independent of the training set by isolating individual mosaics for the validation and test set (Table 1). The test set is tiled up without a tiling window algorithm to avoid double counting predictions on the same image excerpt twice. We indicate in Table 1 which images are used for the training set, the validation set and the test set. In total, we have 932 tiles in the training set, 52 tiles in the validation set and 45 tiles in the test set.

The training set consists of a set of image tiles that are fed to the network in batches (Fig. 3, step (26)). The network uses each batch of image tiles to backpropagate the learnable parameters, which is called one iteration for a single batch. When all available training tiles are fed through the network, one epoch ends. Undifferentiated lineae make up most of the instances in the training set (Fig. 5), and also make up most of the bounding box area (Fig. 4). The feature counts are not independent of each other, since lineaments get cut off randomly by the tiling window algorithm, meaning that a single double ridge can get tiled up into multiple instances of double ridges (compare Fig. 5 to Table B.5).

The training set is imbalanced with regards to the feature count as shown in Fig. 5 and with regards to the feature area as shown in Fig. 4 (note the logarithmic axis). We note that the feature areas are less imbalanced than the feature counts. The imbalance of the training set represents the natural imbalance of linear features on Europa's surface. Inside the Mask R-CNN architecture, only the classification loss of the Mask R-CNN is sensitive to class imbalance. However, an implementation of a weighted loss did not improve the result. We conclude that this class imbalance is not impacting the classification performance due to the fact that classes do not compete in the Mask R-CNN (He et al., 2018). For LineaMapper, this means that one lineament detection can exist multiple times, classified in different categories.

The model was trained for 98 epochs (15,910 iterations, 162 batches, 972 training tiles) in 5.2 h, which is the number of epochs that yielded the best performance on the validation set before the model started to overfit on the training set. Overfitting means that the model learns the training data by heart instead of learning the general concept that it can then apply to unseen data (for example, a two-polynomial fit for three points is an overfit). Most of the training time did not increase the bounding box metrics, but the mask metrics, so the Mask R-CNN needed time to adjust parameters in its mask branch (Fig. 3, steps 16–20).

To prevent the model from overfitting early, we augmented every tile in the training set in every epoch differently, using the *imgaug* (Jung et al., 2020) python library. We used left–right and up–down flipping, shearing, rotation, scaling, contrast enhancing, sharpening and brightness augmenters, pixel inversion, and dropout, applied in a random order and with random parameters. We selected the aforementioned augmenters because they mimic observations of the same area under different viewing geometries or differently processed images from raw spacecraft data. As an aside, these augmenters help make the network robust against such transformations. An example of a randomly augmented training tiles is shown in Fig. 6. Validation and test tiles are

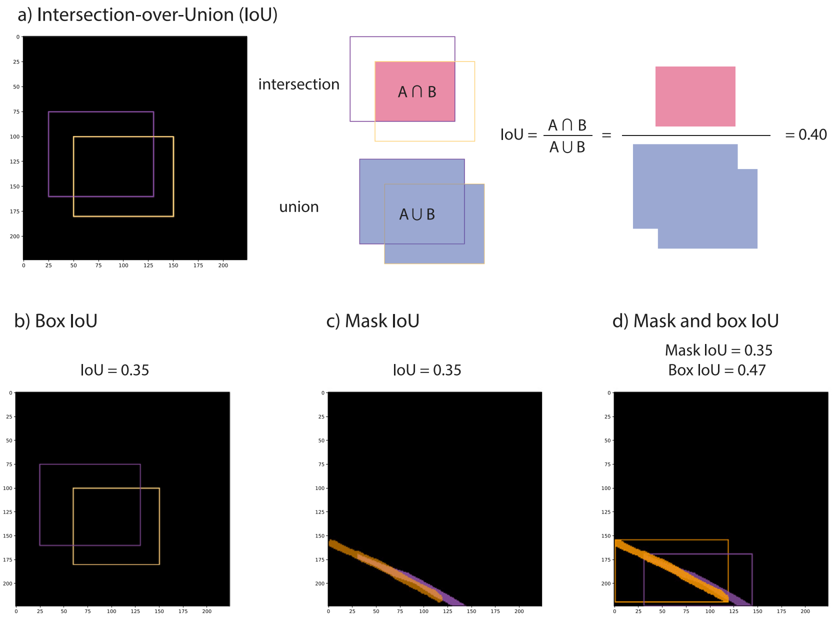

Fig. 7. Introduction of the intersection-over-union (IoU) metric. This is the compact form of Fig. D.17. a) The IoU is the ratio of the intersection of two objects A and B (in this case, two rectangles) over the union of the two objects. (b) An example for an IoU of 0.35 is shown with two rectangles (boxes). (c) An example for an IoU-value of 0.35 is shown for two masks (a mask is a segmented object, in this case a lineament). (d) Examples for both masks and boxes are shown. A box is defined as the rectangle that holds the mask. The examples in (d) show that mask IoU values are in general by design lower than box IoU values.

not augmented. We tested whether the model would overfit without any augmentations and found that it learned the data after 100 epochs.

The validation set is used after each epoch. Undifferentiated lineae are the dominant feature in the validation set (Fig. 5) and make up most of the bounding box area (Fig. 4). To find the best combination of hyperparameters, the model was evaluated on the validation set by comparing model prediction with ground truth. The difference was measured with metrics introduced in Section 2.3.5. This is only used to assess the current model performance. In a way, we overfit on the validation set, since we optimise hyperparameters for best performance on it. In the final training, after the hyperparameters were set, the validation set was added to the training set to maximise training volume. Therefore, we need an additional independent test set, which was not touched until the hyperparameters were fixed. The test set consists of three individual mosaics (Table 1). In 224 × 224 px image tiles, undifferentiated lineae are the most common feature in the test set (Fig. 5) and make up most of the bounding box area (Fig. 4).

2.3.5. Performance metrics

For assessing the performance, we need the number of true positive (TP), false positive (FP) and false negative (FN) detections. Fig. D.19 illustrates the aforementioned quantities for one example tile (Fig. D.18). For object detection and instance segmentation, a true negative (TN) detection is not defined, because an infinite number of not-detected bounding boxes would count as true negative. With TP, FP and FN, the precision is defined as

$$\text{precision} = \frac{\text{TP}}{\text{TP} + \text{FP}} \tag{1}$$

and the recall is defined as

$$\text{recall} = \frac{\text{TP}}{\text{TP} + \text{FN}}. \tag{2}$$

The precision and recall are calculated for one example in Fig. D.20. The precision measures the percentage of truly detected and correctly classified lineaments ratioed by all lineament model detections. The recall measures the percentage of truly detected and correctly classified lineaments ratioed by all ground truth lineaments. Both metrics are invariant to class imbalance. In plain language, high precision means that features the model identifies as lineaments are nearly always real lineaments. However, a model with high precision may be so selective that many lineaments are missed (lots of false negatives). Hence, recall is also used to describe the model. High recall would mean that the model is very good at finding all of the real lineaments. However, a model with high recall that is not very selective would also identify many features that are not actually lineaments (lots of false positives).

To sort detections into true positives, false positives and false negatives, we need to define when a ground truth object is counted as a true detection of the model prediction. Since there will almost never be a perfect detection, we use the intersection-over-union (IoU) metric to define a true-detection criterion:

$$\text{IoU} = \frac{\text{A} \cap \text{B}}{\text{A} \cup \text{B}}$$

with two bounding boxes A and B or two masks A and B (see Fig. 7 for illustrations and examples). We set an IoU threshold above which a predicted bounding box or mask and a ground truth bounding box or mask are considered equal and the model prediction is a true positive. This threshold can be varied. Following He et al. (2018), we use IoU thresholds of 0.35, 0.50, 0.75 and a set of thresholds between 0.50 and 0.95 in steps of 0.05.

Furthermore, the network outputs a score for each detection, which indicates how certain a prediction is (Fig. 3, step (13)). This score, however, is not well calibrated and might therefore not perfectly reflect a linear probability. Still, a higher score means a higher model prediction certainty. Detections are sorted by decreasing score to determine the precision versus recall for a selected IoU threshold (see Fig. D.20 for an example calculation). While decreasing the recall in steps of 0.01, the threshold score, for which a specific recall is achieved, is identified. The area under this precision–recall curve is called average precision, and the mean over all classes is called mean average precision, or mAP (e.g. Beitzel et al., 2009). A precision–recall curve of a perfect model would have a precision of 1 for all recall thresholds and all IoU values. This would result in a mAP of 1, or 100%. The mean average recall, or mAR, is the recall averaged over all classes and over IoU thresholds between 0.5 and 0.95, as for the mAP, unless a single IoU threshold is chosen. An example of calculating mAR and mAP is worked through in Fig. D.20. In the following, we use the mAP and mAR to report model performance

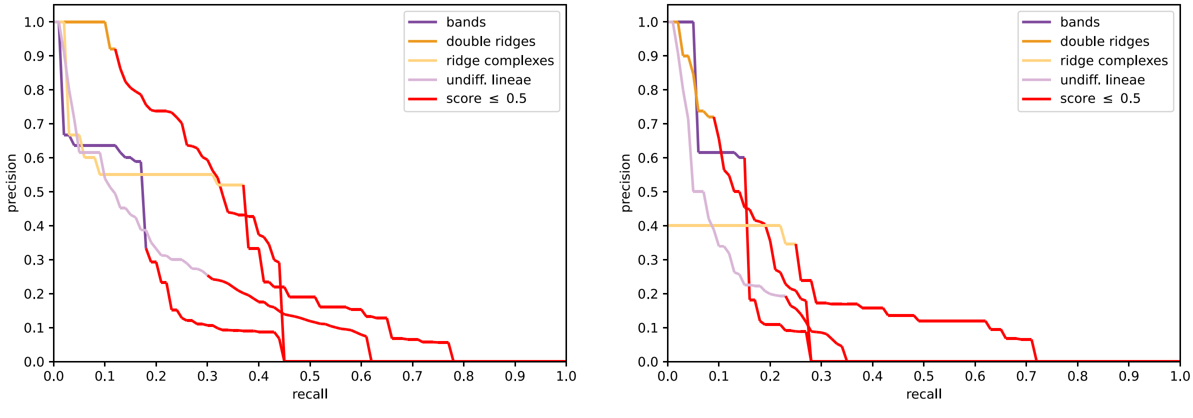

(a)

(b)

Fig. 8. Precision-versus-recall curve for bounding boxes (a) and masks (b). The line turns red if the score falls below 0.5. The IoU-threshold for this curve is 0.5. (For interpretation of the references to colour in this figure legend, the reader is referred to the web version of this article.)

Table 2
Bounding box (bbox) and mask precision and recall for detections with a score higher or equal to 0.5 and at an IoU-threshold of 0.5. The results are displayed in percentage.

	bbox precision	bbox recall	mask precision	mask recall
Bands	33	18	15	8
Double ridges	92	12	68	9
Ridge complexes	50	34	30	17
Undiff. lineae	25	28	15	18
Average	50	23	32	13

results. When no IoU threshold is indicated, we refer to a set of IoU thresholds between 0.5 and 0.95.

3. Performance of LineaMapper

3.1. Performance in metrics

We report results on the test set (Tables 2, 3, 4, and Fig. 8). We start with the precision and recall values at an IoU threshold of 0.5 and a score threshold of 0.5 (Table 2). The precision values (Table 2) are overall higher than the recall values, suggesting that there are fewer false positives than false negatives, meaning that there are more non-detections of actual lineaments than there are false detections of lineaments. This means that a human mapper would have to add more lineaments to the output of LineaMapper than she or he would have to delete. This is true for bands, double ridges and ridge complexes, but not for undifferentiated lineae. On the positive side, the threshold above which output is generated can be tuned individually for each class. This means that we could increase the score threshold to, for example, 70% instead of 50% for undifferentiated lineae to consider only the detections for which the model is more certain that its detection is an undifferentiated lineae.

Furthermore, the metrics make it seem that the model has a harder time correctly applying the mask, i.e. finding the outline of the lineament, than correctly applying a bounding box that encompasses a lineament. However, it is easier for larger objects to achieve a higher IoU, which favours bounding boxes (which are by design bigger than the masks, and much bigger for diagonal lineaments). This relation is visualised in Fig. 7. Therefore, a more qualitative interpretation is important (Section 3.2). Comparing the classes, we find that the model shows the most correct predictions (fewest false positives) for double ridges (highest precision), perhaps due to their clear axial trough, while the most complete detections (fewest false negatives) happen for ridge complexes (highest recall), compared with the ground truth.

The precision–recall curve (Fig. 8) at an IoU threshold of 0.5 allows us to read off the values in Table 2 directly at the point where the line turns red. For example, the line of bounding boxes of double ridges turns from dark orange to red at a precision of 92% and at a recall of 12%. These are the values we find in Table 2. The precision–recall curve visualises how a change in the probability score threshold would lead to different precision and recall values. By tuning the score threshold, we can select a pair of precision/recall values, which we find by following the plotted line in Fig. 8. If we integrate the area under the precision–recall curve in Fig. 8, we would get the average precision values in Tables 3 and 4 for $\mathrm{AP}_{0.50}$. With one glimpse at the area under the curve, we can see why double ridges score highest in the $\mathrm{AP}_{0.50}$ column for both masks and bounding boxes (Tables 3 and 4). To calculate the average precision at an IoU range of 0.50 to 0.95, we would need to plot all precision–recall curves for each IoU threshold (one for 0.50, which we have, one for 0.55, and so on), which is explained in Fig. D.20. We then sum up the areas under those curves and get the 'AP' column in Tables 3 and 4. The average recall 'AR' we calculate by averaging the total recall (score threshold of 0.00) over different IoUs, or only one IoU ($\mathrm{AR}_{0.35}$, $\mathrm{AR}_{0.50}$).

We are now focusing on the performance metrics shown separately for bounding boxes in Table 3 and for masks in Table 4. The class of double ridges reach the overall highest average precision (AP) for masks and bounding boxes. This means that, summed up over all evaluated IoU values, the area under the precision–recall curve was largest for double ridges. This was somewhat expected from the precision discussed above (Table 2). Ridge complexes are the class with the highest average recall (AR), for masks and bounding boxes, which was expected as well from the recall discussion above (Table 2). The worst performing classes, when considering the bounding boxes AP are bands (Table 3), and undifferentiated lineae when considering the masks AP (Table 4). When considering the AR, bands are the worst performing class. Averaged over all classes, the bounding box mAP is 12.1% and the average recall is 31.1%. For masks, the class mean AP is 4.5% and the average recall is 14.6%. As expected from the discussion around Fig. 7, the mAP and AR values are lower for masks than for bounding boxes. We recall that the mAP for an IoU range of 0.5 to 0.95 is a very strict metric. When we look at the mAP at IoU thresholds of 0.5 and of 0.35, we find higher values. In the following, we analyse the results for an IoU threshold of 0.35: The bounding box $\mathrm{mAP}_{0.35}$ is 24.5%, while the $\mathrm{AR}_{0.35}$ is 58.8%. The mask $\mathrm{mAP}_{0.35}$ increases to 14.5%, while the $\mathrm{AR}_{0.35}$ is 41.4%. Again, the mask metrics show lower values simply because of the design of bounding boxes (Fig. 7). Setting the IoU value to 0.35 increased the mean average precision and average recall values by approximately a factor of 2 for bounding boxes and by approximately a factor of 3 for masks.

Table 3

LineaMappper bounding box average precision (AP) and average recall (AR) per class and averaged over classes in percent. The subsets 0.35 and 0.50 indicate an IoU threshold of 0.35 and 0.5, respectively. The subsets S, M and L indicate small, medium and large objects evaluated at an IoU range of 0.50 to 0.95, while no subset evaluates all object sizes at an IoU range of 0.50 to 0.95. Cells are coloured darker (green) with increasing performance.

unit	$AP_{0.35}$	$AP_{0.50}$	AP	AP_S	AP_M	AP_L	$AR_{0.35}$	$AR_{0.50}$	AR	AR_S	AR_M	AR_L
bands	16.4	15.2	9.4	0.6	5.5	22.5	47.3	40.0	24.5	9.0	16.9	43.2
double ridges	32.6	29.3	17.8	6.0	17.2	39.9	46.1	42.8	26.6	10.0	25.9	52.6
ridge complexes	28.4	26.3	11.7	6.5	2.8	27.6	77.1	74.3	42.3	46.7	28.9	60.8
undiff. lineae	20.7	18.4	9.6	2.9	11.0	25.2	64.5	59.4	31.2	17.8	35.2	55.0
mean	24.5	22.3	12.1	4.0	9.1	28.8	58.8	54.1	31.1	20.9	26.7	52.9

Table 4

Same as Table 3, for mask metrics.

unit	$AP_{0.35}$	$AP_{0.50}$	AP	AP_S	AP_M	AP_L	$AR_{0.35}$	$AR_{0.50}$	AR	AR_S	AR_M	AR_L
bands	14.1	4.7	4.1	1.6	1.3	10.5	29.1	18.2	10.2	7.0	7.7	15.3
double ridges	15.9	13.4	6.2	0.5	9.8	9.4	28.3	24.4	11.4	6.9	14.8	9.1
ridge complexes	16.3	8.7	4.2	0.4	1.4	30.8	71.4	54.3	25.1	16.7	22.6	30.8
undiff. lineae	11.8	8.9	3.4	0.3	9.0	7.1	36.7	29.7	11.6	9.2	14.2	6.9
mean	14.5	8.9	4.5	0.7	5.4	14.5	41.4	31.7	14.6	9.9	14.8	15.5

3.2. Qualitative analysis of LineaMapper's predictions

Firstly, we show four examples of model predictions from the test set that showcase the strengths of the current model in Fig. 9. Qualitatively, many undifferentiated lineae are correctly detected by LineaMapper, although sometimes an undifferentiated linea is detected as two individual instances. Even though LineaMapper is not given the full mosaic context, it was able to detect segments of bands. The prediction in Fig. 9.1b of a ridge complex that is overprinted by a double ridge shows that LineaMapper has learned to preserve cross-cutting relationships in some cases. Predictions of the cross-cutting double ridge and undifferentiated linea are scored lower than 0.5 and therefore do not appear in Fig. 9.1b. In Fig. 9.2, the band intersected by an undifferentiated linea was predicted as two individual bands, while the shape is correct. In Fig. 9.3, a double ridge was confused with an undifferentiated lineae, but the correct detection of the double ridge simply scored lower than 0.5. In Fig. 9.4, the network of undifferentiated lineaments was predicted almost perfectly, the double ridge in the upper right corner is classified correctly and the small portion of the band in the upper left corner got segmented and predicted correctly. Inspecting the full test set, we find that predictions by LineaMapper are stable in a sense that the network is not often distracted by other surface features, such as craters or chaos regions.

Secondly, we discuss four examples of model predictions from the test set that showcase the limitations of the current model in Fig. 10. Overall, it seems that LineaMapper indeed finds lineaments, but not the same ones than were mapped in the ground truth. We therefore have a high number of false positives and false negatives. In Fig. 10.1, only half of the band was detected by LineaMapper, while in the other half of the band segment, undifferentiated lineae were predicted by LineaMapper that do not appear in the ground truth. In Fig. 10.2, the model detected only seven lineament instances with a score above 0.5, out of 20 mapped in the ground truth. The model might have been distracted by the densely lineated area observed in 14ESWEDGES01. In Fig. 10.3, a band was confused with a ridge complex. Nonetheless, the cross-cutting relationship was preserved by the model, in contrast to the predicted undifferentiated lineae in the top of Fig. 10.3b, which was additionally confused with a double ridge (Fig. 10.3c). In Fig. 10.4, all double ridges in the ground truth were confused with undifferentiated lineae and one with a ridge complex.

4. Discussion of model performance

We use a test set size of 5% of the total available amount of tiles to maximise the number of tiles available for training. We note that this test set size is slightly smaller than what is usually used for model evaluation, but highlight that previous studies have used a similar approach to mitigate the overall lack of training labels (e.g. Bickel et al., 2022). Nevertheless, we keep in mind that the model performance could vary on a different test set.

4.1. Metrics

The metrics show that LineaMapper has learned how to identify a lineament and apply it to new data. The masks of undifferentiated lineae are supposedly under-performing because of their small size and their geometric relationship to double ridges. If a detection is classified as an undifferentiated linea instead of a double ridge, the prediction counts as a false positive for undifferentiated lineae and a false negative for double ridges. This would decrease the precision of undifferentiated lineae and decrease the recall for double ridges, in line with the performance for double ridges and undifferentiated lineae.

Small objects, i.e. objects with a bounding box below 32 × 32 pixel, show on average the lowest performance, for bounding box and mask AP and AR. Small objects perform also worst on the COCO test set, because of the scarcity of small objects in the training data. This could be mitigated by model adjustments (Kisantal et al., 2019).

If each mosaic in the test set is analysed individually (Tables C.6 to C.11), we find that 17ESREGMAP01EXCERPT1 shows by far the best performance metrics, reaching an AP at IoU of 0.35 of 42.2% for the bounding boxes and 35.9% for the masks and an AR at IoU of 0.35 of 79.5% for the bounding boxes and 53.1% for the masks. The mosaic 17ESREGMAP01EXCERPT1 is the closest to the training and validation data mosaics 17ESREGMAP01EXCERPT2 and 17ESREGMAP03, since it was acquired in the same encounter with similar observing geometries. This shows that the performance of LineaMapper is better for similarly acquired data. It also shows why an independent test set is important.

For the selected case shown in Table 2, the precision is on average higher than the recall, which means that we have more false negatives than false positives. The precision–recall curve in Fig. 8 shows that for a decreasing score, the recall increases (less false negatives) and the precision decreases (more false positives). Especially for double ridges, the bounding boxes could reach, for example, a recall of 30% for a precision of 50% if the score threshold would be lowered. However, for other classes, lowering the score threshold would not be beneficial for the precision. Because the score threshold can be varied, it can be set according to specific needs.

The performance of LineaMapper is impacted by two main factors, besides the scarcity of training data. Firstly, the test set is independent

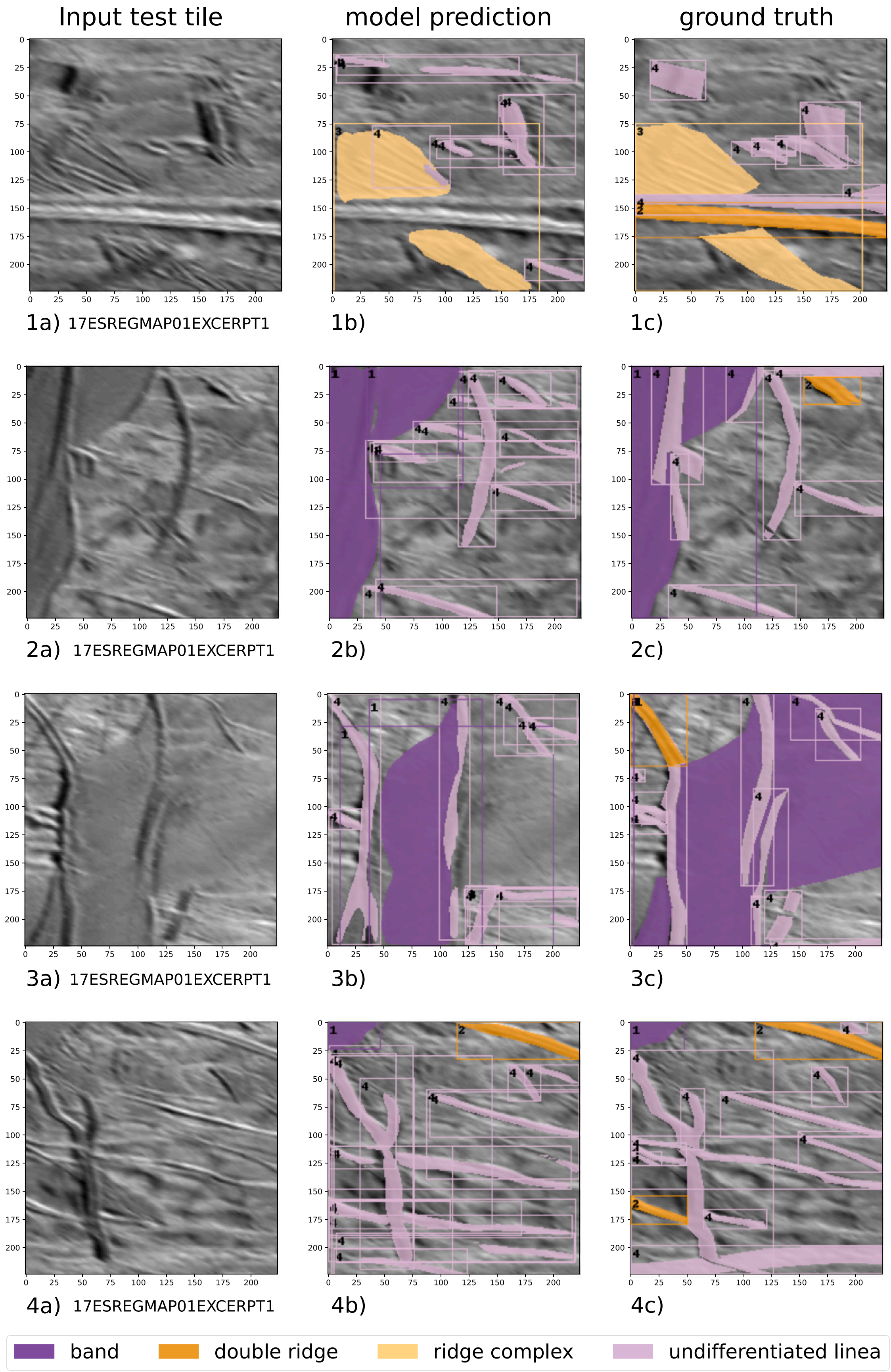

Fig. 9. Example results from the test set showcasing LineaMapper's strength. Column (a) shows the input test tile. Column (b) contains LineaMapper predictions for probability scores above 0.5. The ground truth is shown for comparison in column (c). Bands (1) are shown in purple, double ridges (2) in dark orange, ridge complexes (3) in light orange and undifferentiated lineae (4) in pale pink. (For interpretation of the references to colour in this figure legend, the reader is referred to the web version of this article.)

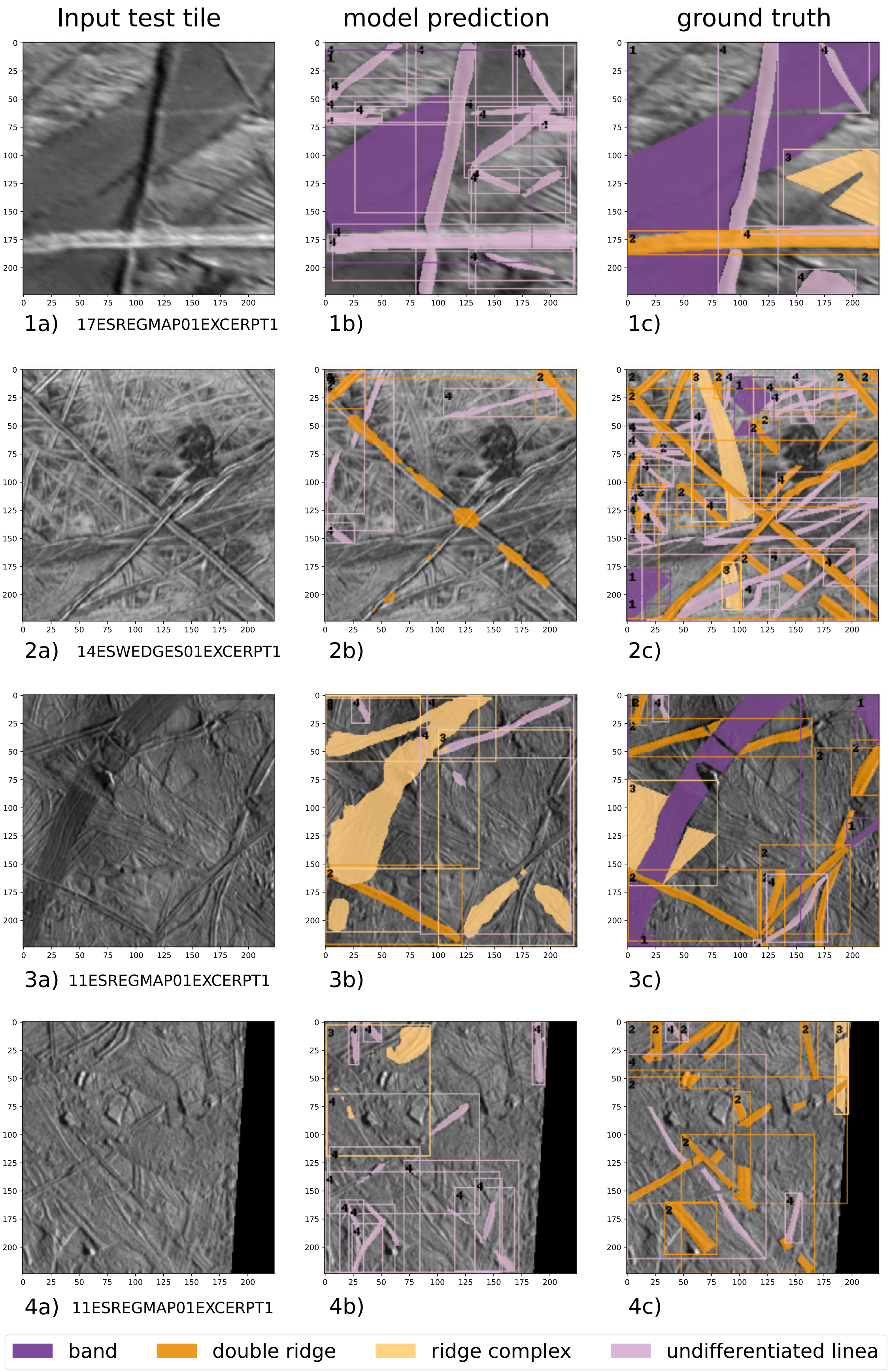

1a) 17ESREGMAP01EXCERPT1 1b) 1c)

2a) 14ESWEDGES01EXCERPT1 2b) 2c)

3a) 11ESREGMAP01EXCERPT1 3b) 3c)

4a) 11ESREGMAP01EXCERPT1 4b) 4c)

Fig. 10. Example results from the test set showcasing LineaMapper's limitations. Column (a) shows the input test tile. Column (b) contains LineaMapper predictions for probability scores above 0.5. The ground truth is shown for comparison in column (c). Bands (1) are shown in purple, double ridges (2) in dark orange, ridge complexes (3) in light orange and undifferentiated lineae (4) in pale pink. (For interpretation of the references to colour in this figure legend, the reader is referred to the web version of this article.)

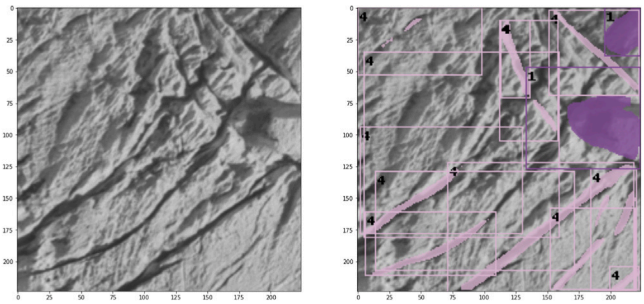

Fig. 11. Crevasses on the Aletsch glacier, Switzerland. left: Screenshot of an aerial view of the Aletsch glacier. The excerpt shows an area of 98 × 98 meters at a resolution of 0.5 m/px, which is the highest resolution that EIS NAC will achieve. (Data from the Federal Office of Topography swisstopo). right: Prediction of LineaMapper. The crevasses are classified by LineaMapper as undifferentiated lineae, while two glacier fragments are classified as bands.

of the training and validation set, almost mimicking data from a different spacecraft, which makes the task harder. Secondly, segmenting lineaments almost down to the noise level in Galileo SSI data is a challenging task, even for a human (Fig. 1). Given these factors, the performance metrics provide a lower limit to the actual performance of LineaMapper.

4.2. Qualititative interpretation

The predictions on the test set show that LineaMapper is comprehensibly predicting and classifying linear surface features, and sometimes even detects cross-cutting relationships, although it is not yet highly skilled at generalising predictions to unknown areas imaged under conditions it has not been trained on. The predictions are comprehensible in a sense that a human can retrace why the network made a mistake. For example, LineaMapper confuses ridge complexes often with bands, and double ridges with undifferentiated lineae, which the human mapper struggled with as well. It is therefore unsurprising that undifferentiated lineae, when resolved better, often turn out as double ridges. Interestingly, we see in the example of the logit masks (Fig. 3, in step 19) that masks with labels 1 (bands) and 3 (ridge complexes) contain almost identical values, and masks with labels 2 (double ridges) and 4 (undifferentiated lineae) are also almost identical. This shows that, at least in the mask branch, bands are treated the same as ridge complexes and double ridges are treated the same as undifferentiated lineae. For the connection between ridge complexes and double ridges, there is an ongoing debate whether they have a different (Aydin, 2006) or the same (Manga and Sinton, 2004) formation mechanism. Visually, in some ridge complexes, individual double ridges are clearly identifiable (e.g. second row in Fig. 1), while in others not (e.g. first and third row in Fig. 1). Furthermore, the logit masks in step (19) (Fig. 3) show that the mask branch has problems with disentangling individual lineaments. Perhaps, this issue could be diminished with a synthesised training set, where instances are cropped out of the tile and implanted into an environment without entanglements. However, it might be that indeed because of the detection of multiple instances in one mask, the cross-cutting relationships can sometimes be respected by LineaMapper.

5. Conclusion

LineaMapper provides reasonable and valuable predictions, which makes it a helpful and much needed tool for mapping lineaments on Europa. Almost every detection, regardless of the score, is reasonable. Sometimes, LineaMapper even suggests an additional lineament that is not represented in the ground truth, perhaps due to length, width or contrast constraints. This is an important result as this would improve the performance metrics due to a higher number of true positives and a lower number of false positives. More importantly, it shows the difficulty of mapping lineaments completely and correctly, even for a human.

One strength of LineaMapper is the possibility to be retrained with additional data. Not only will this help to map lineaments in Europa Clipper EIS data, but it can also be retrained for similar looking linear surface features on other planetary objects, as was shown for a similar application by Bickel et al. (2020b). Another strength is the that the output of LineaMapper can be tuned by setting different thresholds, such as the mask threshold for the conversion from float to binary masks, or the probability score threshold (see Fig. 3). The biggest strength, however, is the speed with which LineaMapper can produce predictions: 15 ms per 224 × 224 tile on average.

The current version of LineaMapper has limitations, which can be improved in subsequent versions. The major limitation of LineaMapper v1.0 is that it is trained on a subset of Galileo data in the resolution range of 150 to 600 m/px. Therefore, we do not have a good handle on the model performance outside of this resolution range. This is especially important for higher resolution images expected with EIS on Europa Clipper. For a lower resolution image, lineaments are, in the worst case, classified as undifferentiated lineae by the network, while in a higher resolution image, the defined unit identifiers might change and can lead to misclassified lineaments or to an increasing number of false positives.

6. Summary

We train LineaMapper v1.0, a neural network to segment instances of four categories of lineaments in Galileo images of Europa. We pave the way to a faster and more deterministic mapping of linear surface features on Europa. LineaMapper v1.0 allows global analysis of linear surface features in a reasonable time frame. The detected bounding boxes and their predicted masks facilitate parameter extraction, such as length, width, and azimuth of an individual lineament. LineaMapper v1.0 shows the potential for an automatic analysis of cross-cutting relationships, since it is in some cases able to preserve the cross-cutting relationships. In terms of performance metrics, LineaMapper v1.0 has a mean average precision of 22.3% (bounding boxes) and 8.9% (masks) and a mean average recall of 54.1% (bounding boxes) and 31.7% (masks), both at an IoU of 0.5. Given the complexity of the problem and considering human mapping biases, this is an adequate performance.

7. Outlook

In the light of Europa Clipper, calibration parameters from EIS WAC and NAC can be used as augmenters for the next version of LineaMapper to prepare it for data from a new spacecraft and unknown regions of Europa. To further prepare LineaMapper for Europa Clipper EIS data, superresolution neural networks could be trained to enhance the Galileo data set and to simulate a larger high-resolution data set. Additionally, terrestrial analogues (such as terrestrial glaciers or the polar ice sheets) that have been imaged at the resolution we are expecting from EIS could be used for training. One such example is given in Fig. 11. Additionally, LineaMapper output can be georeferenced, which is valuable for recurring updates of a detailed, global map of lineaments on Europa. Such a georeferencing workflow could be envisaged by an implementation into a GIS tool, for example as a plugin in QGIS. During Europa Clipper flybys, a quick feature extraction would be valuable for change detection, either since Galileo or between Europa Clipper flybys. At the same time, such a framework would facilitate the extraction of spectra from Europa Clipper's Mapping Imaging Spectrometer for Europa (MISE) data (Blaney et al., 2022).

Naturally, the model training would benefit from a bigger training set that includes a wider resolution range. Since manual segmentation is a slow and cumbersome process, we envision an extended training

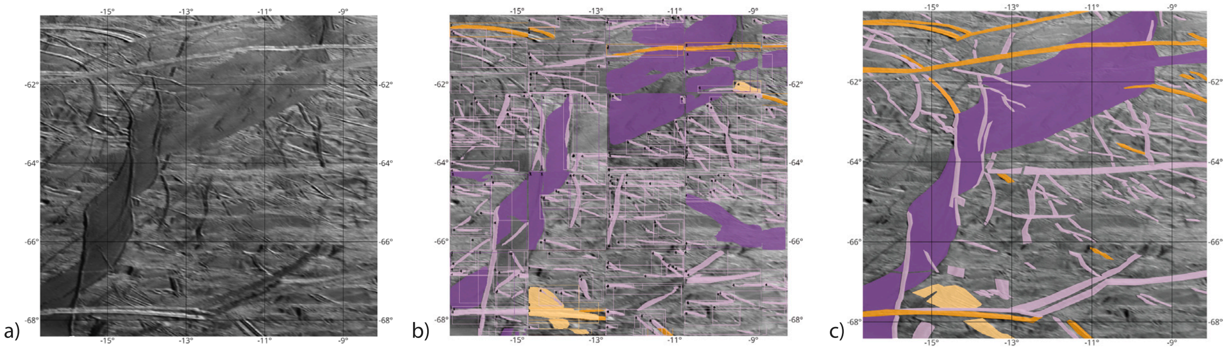

Fig. 12. An outlook of a full 800 × 800 mosaic georeferenced model prediction. (a) The input black-and-white Galileo image (17ESREGMAP01EXCERPT1; Table 1). (b) For this full-mosaic prediction, the individual predictions of LineaMapper on 224 × 224 tiles are simply puzzled together. A stitching algorithm is needed to join predictions of the same lineament. (c) For comparison, the ground truth manual map is shown. Bands (1) are shown in purple, double ridges (2) in dark orange, ridge complexes (3) in light orange and undifferentiated lineae (4) in pale pink. Projection is east-positive equirectangular. (For interpretation of the references to colour in this figure legend, the reader is referred to the web version of this article.)

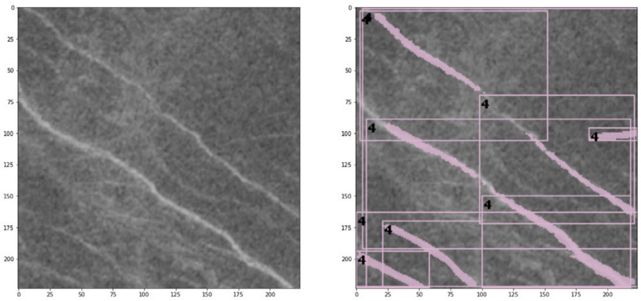

Fig. 13. Wrinkle ridges on Venus. Left: Left look of a Magellan SAR black-and-white input image resized from 100 × 100 px to 224 × 224 px (original resolution: 75 m/px, 7.5 km total width displayed). The projection is equirectangular and this excerpt is located roughly at 99° East and 21° South. Data from USGS (Ford et al., 1989, 1993). Right: Prediction of LineaMapper. The undifferentiated lineae category is essentially an arbitrary line detector.

set by using LineaMapper v1.0 to reduce the segmentation workload for a human mapper. In future work, we plan to cleanse LineaMapper's output on the full regional mosaics. This leaves us with a bigger training set and, at the same time, provides a new lineament map revealing unprecedented detail. The making of a global lineament map using all available imaging data is our final goal. We are going to encompass this with LineaMapper v2.0, which is going to be trained on the basis of the cleansed regional mosaics. Furthermore, we need an algorithm that joins the model predictions, which are output in small tiles, together. This is showcased in Fig. 12.

Finally, it is conceivable that LineaMapper can be fine tuned andapplied to similar looking features such as wrinkle ridges on Venus, scarps on Mercury, grooves and furrows on Ganymede (Fig. E.21) or dust devil tracks on Mars. A preliminary test for wrinkle ridges on Venus in left look Magellan Synthetic Aperture Radar (SAR) imagery data has shown promising results (Fig. 13).

Declaration of competing interest

The authors declare that they have no known competing financial interests or personal relationships that could have appeared to influence the work reported in this paper.

Data availability

We share the code we wrote for this project, the model weights, the training log files, performance assessment and the training, validation and test data set through Mendeley data. The full manual segmentations are available upon request.

> LineaMapper: a deep learning-powered tool for mapping linear surface features on Europa (Haslebacher et al., Icarus, 2023) accompanying data (Original data) (Mendeley Data)

Acknowledgements

This work has been carried out within the framework of the National Centre of Competence in Research PlanetS supported by the Swiss National Science Foundation under grants 51NF40_182901 and 51NF40_205606. The authors acknowledge the financial support of the SNSF.

Valentin T. Bickel is funded by the Center for Space and Habitability at the University of Bern.

We are thankful for input from Dr. Elizabeth 'Zibi' Turtle and Dr. Pablo Marquez-Neila. We thank the two anonymous reviewers for their valuable suggestions.

Appendix A. Guideline for manual segmentation

See Fig. A.14.

Appendix B. Fully segmented images with feature count

See Figs. B.15 and B.16.

Appendix C. Performance on individual mosaics

See Tables C.6–C.11.

Appendix D. Machine learning basics - explanatory figures

See Figs. D.17–D.20.

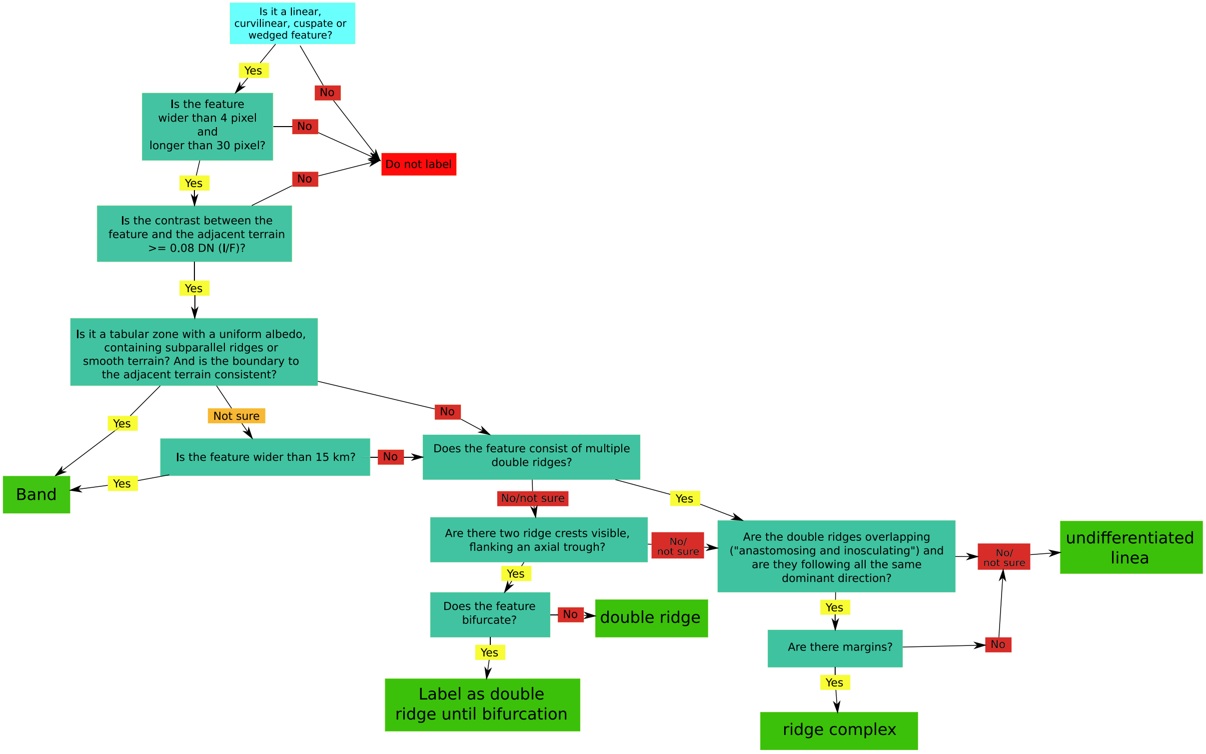

Fig. A.14. Guideline for manual segmentation.

Table B.5
Count of ground truth features in each observation.

Observation ID	Total number	Bands	Double ridges	Ridge complexes	Undifferentiated Lineae
11ESCOLORS01-01	41	0	4	5	32
11ESREGMAP01EXCERPT1	142	12	49	12	69
12ESFRTPLT01EXCERPT1	43	5	15	2	21
14ESWEDGES01EXCERPT1	57	4	18	3	32
15ESREGMAP01EXCERPT1	108	4	11	4	89
17ESREGMAP01EXCERPT1	101	2	14	1	84
17ESREGMAP01EXCERPT2	99	7	9	1	82
17ESREGMAP03	260	20	4	10	226
25ESDARKBP01	112	3	19	5	85
E4ESMACSTR01	37	1	0	0	36
E6ESDRKLIN01	678	45	81	56	496
G7ESAPEXCR01	12	0	1	1	10
G7ESAPEXCR02	10	0	1	1	8
G7ESAPEXCR04	41	2	5	0	34
G7ESAPEXCR05	48	0	4	2	42
G7ESLOWFOT01	12	1	0	0	11
G7ESTYRMAC01	17	0	0	0	17
G7ESTYRMAC02	18	0	0	0	18
Sum	1836	106	235	103	1392

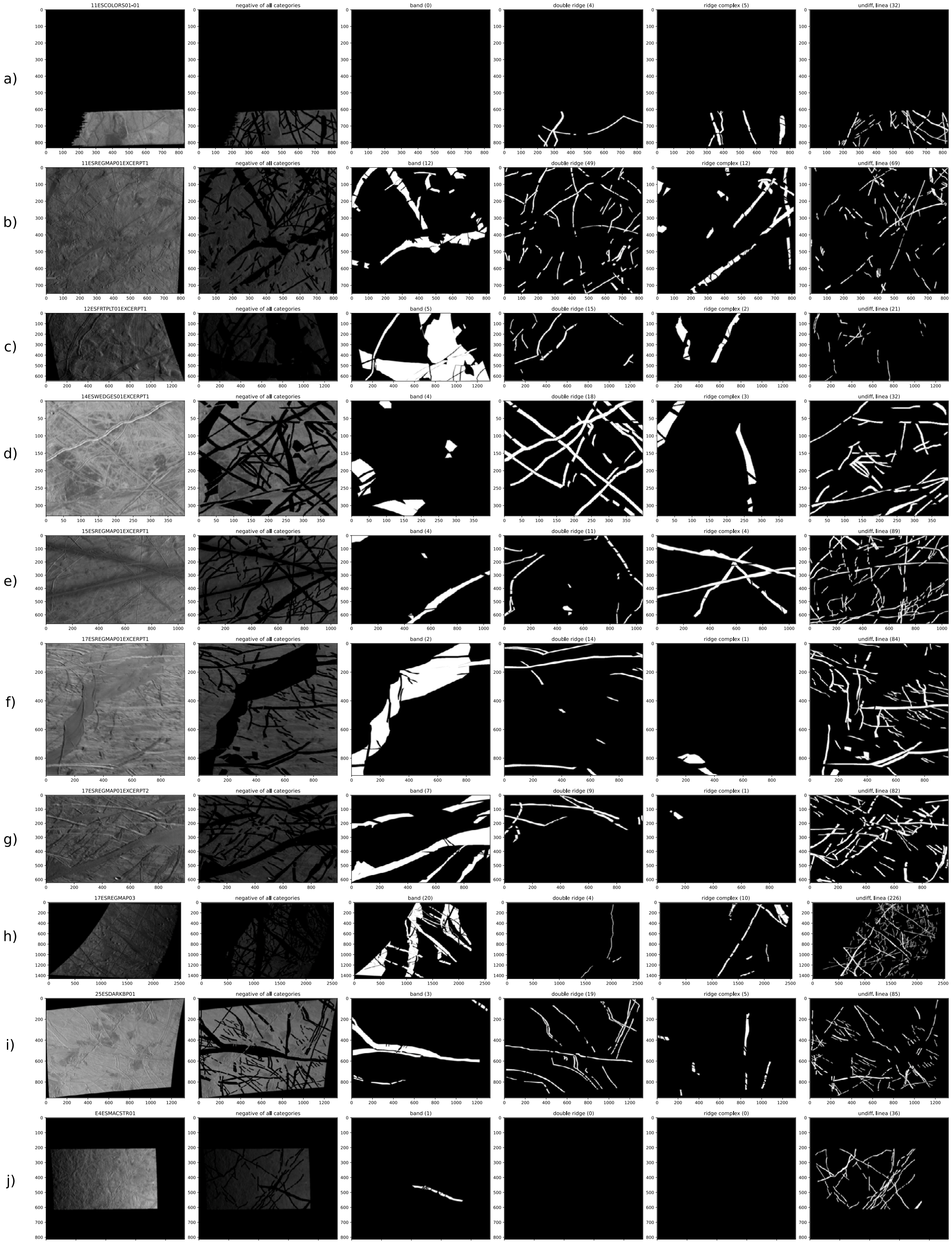

Fig. B.15. Masks of segmented Galileo mosaics, separately displayed for the units (bands, double ridges, ridge complexes, undifferentiated lineae).

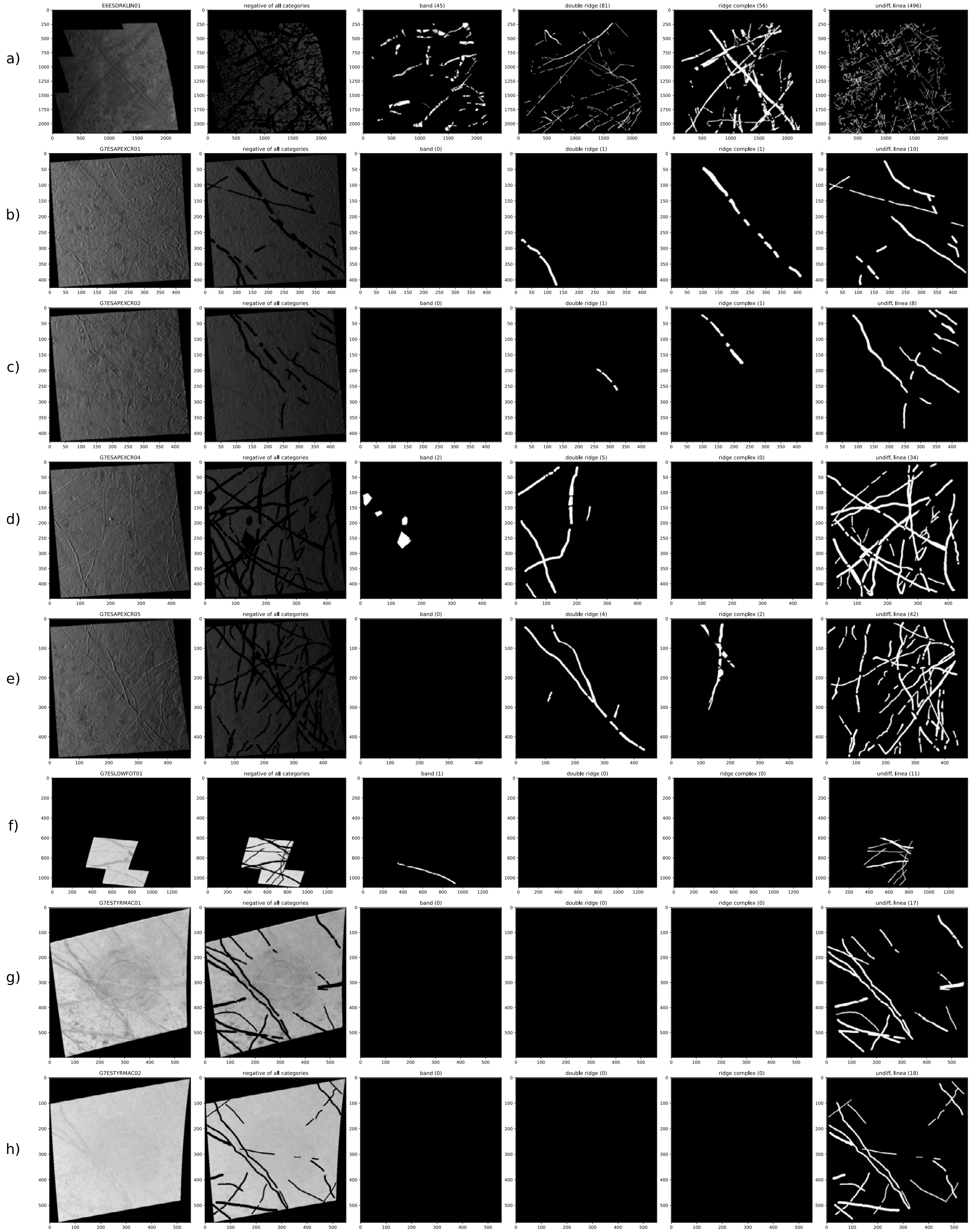

Fig. B.16. Masks of segmented Galileo mosaics, separately displayed for the units (bands, double ridges, ridge complexes, undifferentiated lineae).

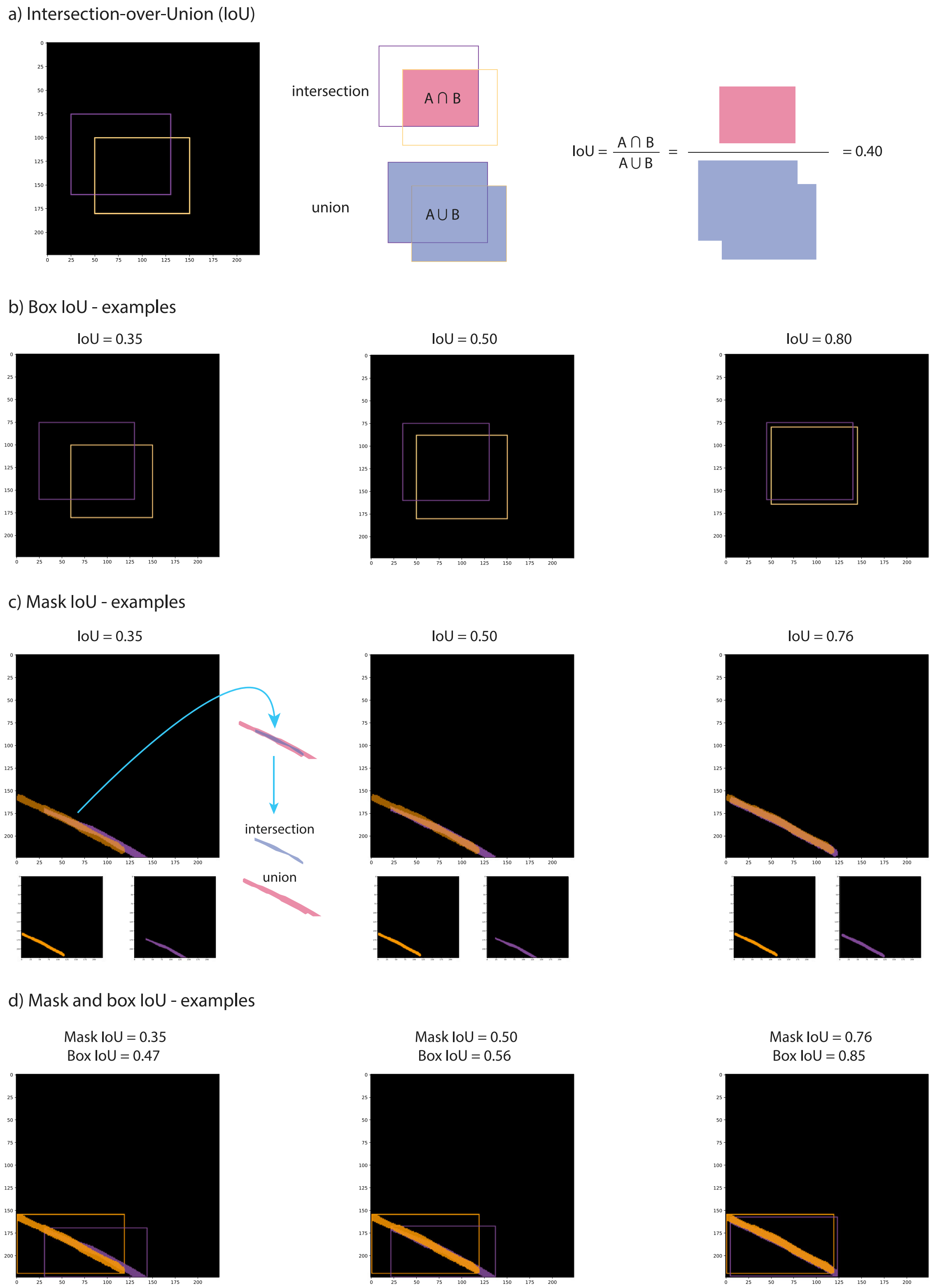

Fig. D.17. Introduction of the intersection-over-union (IoU) metric. (a) The IoU is the ratio of the intersection of two objects A and B (in this case, two rectangles) over the union of the two objects. (b) Examples for an IoU of 0.35, an IoU of 0.50 and an IoU of 0.80 are shown with two rectangles (boxes). (c) Example IoU-values of 0.35, 0.50 and 0.76 are shown for two masks (a mask is a segmented object, in this case a lineament) are displayed, with the individual masks underneath for clarity. (d) Examples for both masks and boxes are shown. A box is defined as the rectangle that holds the mask. The examples in (d) show that mask IoU values are in general by design lower than box IoU values.

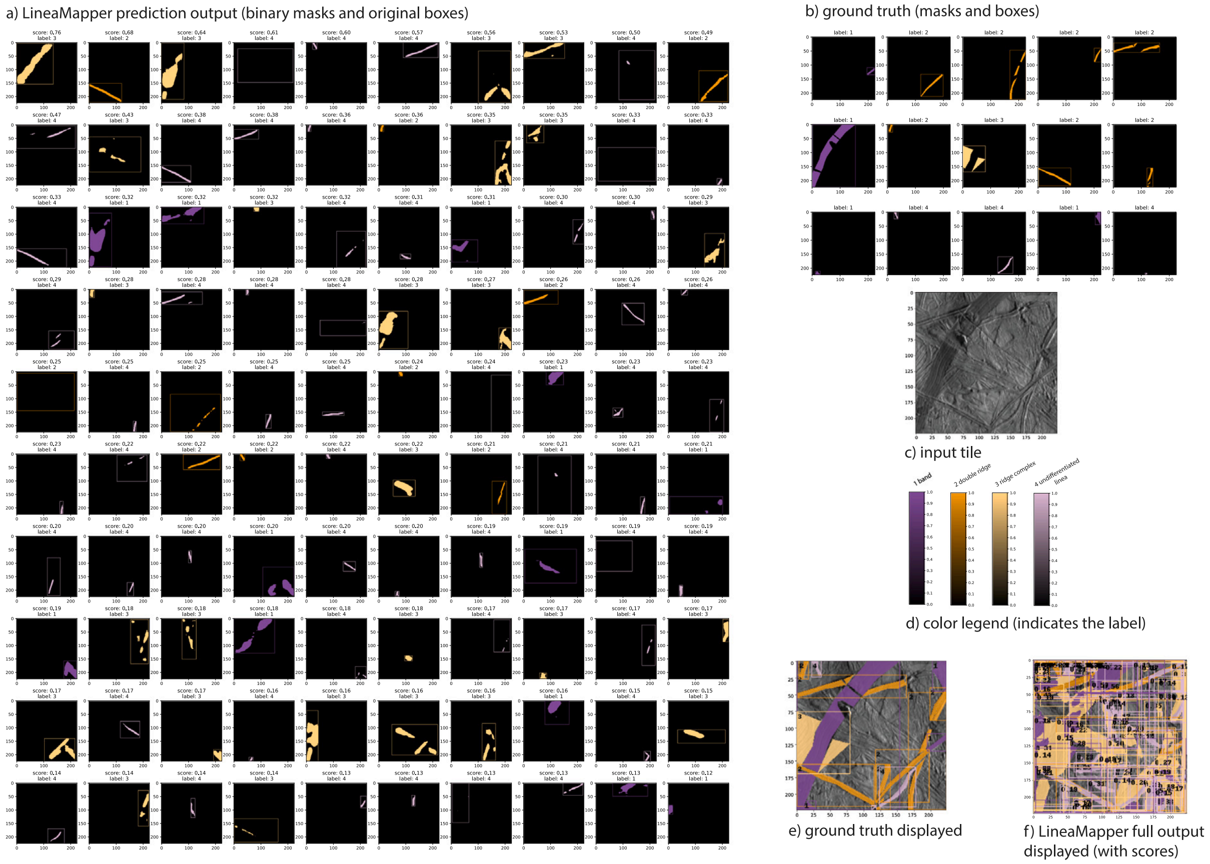

Fig. D.18. Full output of LineaMapper (maximal detections are set to 100) and the ground truth for one input test tile. (a) 100 detections of LineaMapper shown as binary masks (mask threshold = 0.5) with their original boxes. The plots are sorted in descending order of probability scores, from left to right in rows from top to bottom. (b) The ground truth masks are shown with their label and bounding box (computed from the mask). (c) The input tile. (d) The colour legend for the labels classifying the geological unit. (e) The ground truth mappings (b) displayed on top of the input tile. (f) The full output of LineaMapper (a) displayed on top of the input tile.

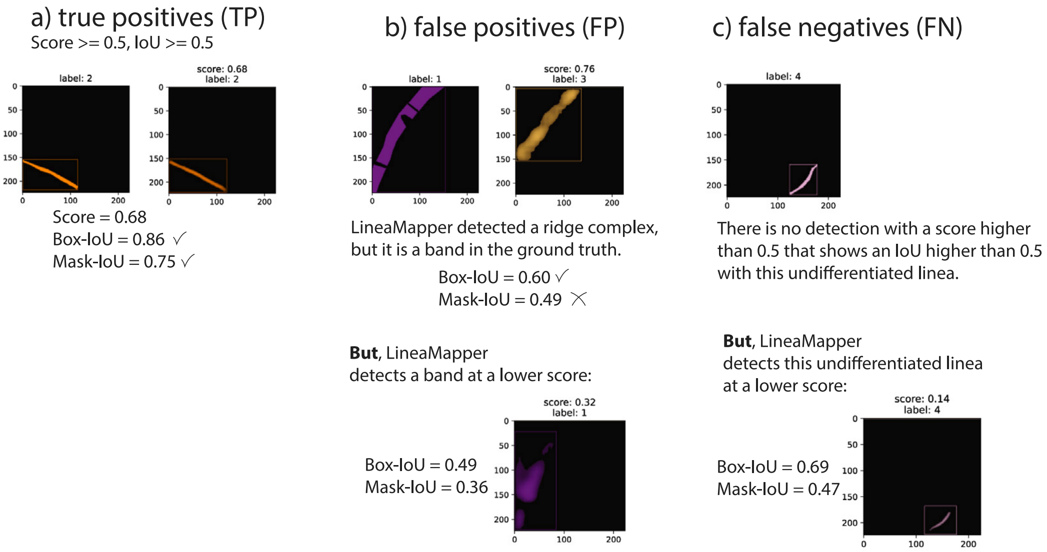

Score = 0.68
Box-IoU = 0.86 ✓
Mask-IoU = 0.75 ✓

LineaMapper detected a ridge complex, but it is a band in the ground truth.
Box-IoU = 0.60 ✓
Mask-IoU = 0.49 ✗

But, LineaMapper detects a band at a lower score:
Box-IoU = 0.49
Mask-IoU = 0.36

There is no detection with a score higher than 0.5 that shows an IoU higher than 0.5 with this undifferentiated linea.

But, LineaMapper detects this undifferentiated linea at a lower score:
Box-IoU = 0.69
Mask-IoU = 0.47

Fig. D.19. Examples of true positives (a), false positives (b) and false negatives (c) for an IoU threshold of 0.5 and a score threshold of 0.5. Examples come from Fig. D.18.

How to calculate the metrics (precision, recall, mean average precision (mAP) and average recall (AR))

1 Select one of:

- boxes
  - bands
  - double ridges
  - ridge complexes
  - undifferentiated lineae
- masks
  - bands
  - double ridges
  - ridge complexes
  - undifferentiated lineae

2 choose an IoU threshold, for example
IoU ≥ 0.5

3 sort into true positive (TP), false negative (FN)
and false positive (FP)

4 evaluate precision and recall at a
selected score threshold, e.g.
score ≥ 0.5

5 for decreasing score thresholds, calculate
precision and recall and plot these points
in a precision-recall curve

6 The integral of the precision-recall curve
gives the 'average precision' (AP) for the selected
choices.

example of a precision-recall curve

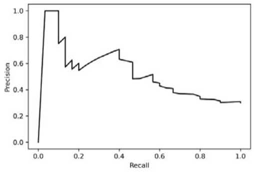

7 The average recall (AR) is calculated as the average over a set of
IoU-thresholds (standard: 0.50, 0.55, 0.60, ..., 0.90, 0.95) or a single IoU.

Example

1 Selection:
boxes
- double ridges (label=2)

2 Selected IoU threshold: IoU ≥ 0.5

3 We evaluate true positive (**TP**), false negative (FN)
and false positive (**FP**)

3.1 We first plot a table with the box IoU between all LineaMapper predictions that are labelled as 'double ridge' and all 'double ridge' targets (target = ground truth mappings).

		TP prediction 1 score: 0.68	**TP** prediction 9 score: 0.49	**TP** prediction 15 score: 0.36	**TP** prediction 37 score: 0.26	**FP** prediction 40 score: 0.25	**FP** prediction 42 score: 0.25	**FP** prediction 45 score: 0.24	**FP** prediction 52 score: 0.22	**FP** prediction 53 score: 0.22	**FP** prediction 56 score: 0.21
	target 1	0.017	0.52	0	0	0.028	0.24	0	0	0	0.39
FN	target 2	0	0.38	0	0	0.14	0.26	0	0.033	0	0.41
FN	target 3	0	0	0	0	0.028	0.0048	0	0.042	0	0
	target 4	0	0	0.01	0.55	0.19	0	0	0.26	0.0089	0
	target 6	0	0	0.73	0.049	0.0096	0	0	0	0	0
	target 8	0.86	0.0074	0	0	0	0.18	0	0	0	0
FN	target 9	0.022	0.11	0	0	0	0.055	0	0	0	0

*Enumeration starts at 0; increasing with ascending score for predictions; random order for targets. See Figure of full output.

3.2 The IoU-values that satisfy our IoU threshold are highlighted in red. The corresponding predictions are **true positives (TP)**, since these predictions match one target.

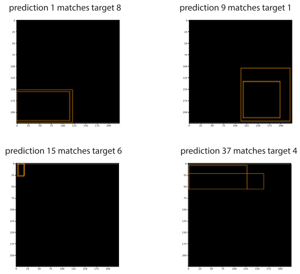

3.3 Targets 2, 3 and 9 do not have a matching model prediction.
Therefore, these are non-detections = **false negatives (FN).**

3.3 Predictions 40, 42, 45, 52, 53 and 56 do not have a matching target.
Therefore, these are false model detections = **false positives (FP).**

4 We evaluate precision and recall at a selected score threshold: score ≥ 0.5
We go and check in the full output for the prediction scores. We see that only predictions 0 to 8 have a score higher than 0.5. This leaves us with:

TP = 1
FN = 3
FP = 0

$$\text{Precision} = \frac{\mathbf{TP}}{\mathbf{TP} + \mathbf{FP}} = \frac{\mathbf{1}}{\mathbf{1} + \mathbf{0}} = \mathbf{1}$$

$$\text{Recall} = \frac{\mathbf{TP}}{\mathbf{TP} + \mathbf{FN}} = \frac{\mathbf{1}}{\mathbf{1} + \mathbf{3}} = \mathbf{0.25}$$

5 For decreasing score thresholds, we calculate
precision and recall and plot these points
in a precision-recall curve (in step 6).

score threshold	0.9	0.8	0.7	0.6	0.5	0.4	0.3	0.26	0.25	0.24	0.22	0.21
TP	0	0	0	1	1	2	3	4	4	4	4	4
FP	0	0	0	0	0	0	0	0	2	3	5	6
FN	3	3	3	3	3	3	3	3	3	3	3	3
Recall	**0**	**0**	**0**	**0.25**	**0.25**	**0.40**	**0.50**	**0.57**	**0.57**	**0.57**	**0.57**	**0.57**
Precision	**na**	**na**	**na**	**1.00**	**1.00**	**1.00**	**1.00**	**1.00**	**0.67**	**0.57**	**0.44**	**0.40**

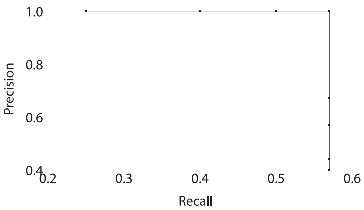

6 We calculate the 'average precision' (AP) as the integral of the precision-recall curve and get an AP of 0.32 for the bounding boxes of double ridges.

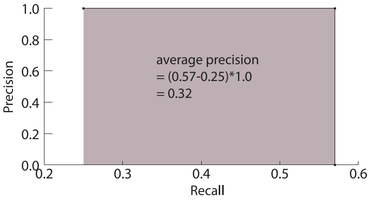

7 Here, we calculate the average recall (AR) as the average over a set of
IoU-thresholds: (0.50, 0.55, 0.60, ..., 0.90, 0.95). All detections
are taken into account. We get an AR of 0.16.

IoU threshold	0.50	0.55	0.60	0.65	0.70	0.75	0.80	0.85	0.90	0.95	**average Recall (AR):**
TP	4	3	2	2	2	1	1	1	0	0	
FP	6	7	8	8	8	9	9	9	10	10	
Recall	0.40	0.30	0.20	0.20	0.20	0.10	0.10	0.10	0.00	0.00	**0.16**

Fig. D.20. Precision and recall metrics explained in detail and showcased on one example.

Table C.6
Same as Table 3 for bounding boxes in **14ESWEDGES01EXCERPT1**.

unit	$AP_{0.35}$	$AP_{0.50}$	AP	AP_S	AP_M	AP_L	$AR_{0.35}$	$AR_{0.50}$	AR	AR_S	AR_M	AR_L
bands	2.6	1.0	1.0	0.0	1.8	0.0	25.0	12.5	11.3	0.0	18.0	0.0
double ridges	48.8	45.3	31.6	5.4	24.5	58.2	53.5	51.2	35.8	5.0	30.6	62.7
ridge complexes	34.8	31.4	23.7	70.2	3.1	80.0	80.0	80.0	54.0	70.0	25.0	80.0
undiff. lineae	15.3	14.9	7.3	3.4	11.0	17.9	44.4	42.9	22.9	6.5	30.3	67.5
mean	25.4	23.1	15.9	19.8	10.1	39.0	50.7	46.6	31.0	20.4	26.0	52.5

Table C.7
Same as Table 3 for masks in **14ESWEDGES01EXCERPT1**.

unit	$AP_{0.35}$	$AP_{0.50}$	AP	AP_S	AP_M	AP_L	$AR_{0.35}$	$AR_{0.50}$	AR	AR_S	AR_M	AR_L
bands	1.0	1.0	0.2	0.0	0.4	0.0	12.5	12.5	2.5	0.0	4.0	0.0
double ridges	13.8	13.8	6.3	1.1	4.9	12.9	23.3	23.3	10.2	4.0	11.7	12.7
ridge complexes	45.0	34.8	15.6	8.7	4.7	50.0	100.0	80.0	32.0	25.0	30.0	50.0
undiff. lineae	9.6	7.8	2.8	0.7	10.5	0.0	19.0	15.9	6.5	1.9	10.9	0.0
mean	17.3	14.3	6.2	2.6	5.1	15.7	38.7	32.9	12.8	7.7	14.1	15.7

Table C.8
Same as Table 3 for bounding boxes in **11ESREGMAP01EXCERPT1**.

unit	$AP_{0.35}$	$AP_{0.50}$	AP	AP_S	AP_M	AP_L	$AR_{0.35}$	$AR_{0.50}$	AR	AR_S	AR_M	AR_L
bands	6.8	5.8	3.3	0.0	0.5	18.9	35.5	25.8	11.6	0.0	10.0	27.1
double ridges	22.4	18.8	11.0	6.6	10.4	27.8	38.5	34.6	20.3	10.8	16.9	47.4
ridge complexes	27.0	24.6	9.4	0.0	3.4	20.9	73.1	69.2	36.2	0.0	27.3	53.0
undiff. lineae	11.2	9.2	4.2	7.7	2.1	9.8	58.9	54.2	25.8	23.1	24.1	40.7
mean	16.8	14.6	7.0	3.6	4.1	19.4	51.5	46.0	23.5	8.5	19.6	42.1

Table C.9
Same as Table 3 for masks in **11ESREGMAP01EXCERPT1**.

unit	$AP_{0.35}$	$AP_{0.50}$	AP	AP_S	AP_M	AP_L	$AR_{0.35}$	$AR_{0.50}$	AR	AR_S	AR_M	AR_L
bands	2.7	0.8	0.5	0.3	0.1	8.9	16.1	9.7	3.9	2.9	2.4	8.6
double ridges	12.3	8.2	4.0	0.6	9.4	7.0	24.0	19.2	8.9	7.3	11.0	6.8
ridge complexes	12.6	5.0	2.5	0.0	1.7	21.4	69.2	50.0	22.3	0.0	24.7	21.0
undiff. lineae	2.9	2.1	0.6	0.7	4.7	0.0	25.2	19.6	6.3	8.8	5.1	0.0
mean	7.6	4.0	1.9	0.4	4.0	9.3	33.7	24.6	10.3	4.8	10.8	9.1

Table C.10
Same as Table 3 for bounding boxes in **17ESREGMAP01EXCERPT1**.

unit	$AP_{0.35}$	$AP_{0.50}$	AP	AP_S	AP_M	AP_L	$AR_{0.35}$	$AR_{0.50}$	AR	AR_S	AR_M	AR_L
bands	44.2	43.0	28.0	11.3	35.5	31.5	81.2	81.2	56.2	90.0	45.0	57.3
double ridges	40.1	39.4	21.8	3.9	27.8	0.0	60.6	57.6	34.2	15.0	38.2	0.0
ridge complexes	53.1	53.1	44.0	-100.0	1.8	85.0	100.0	100.0	67.5	-100.0	45.0	90.0
undiff. lineae	31.3	28.1	15.3	2.1	16.0	40.4	76.2	69.4	38.0	18.2	41.3	63.3
mean	42.2	40.9	27.3	5.7	20.3	39.2	79.5	77.1	49.0	41.1	42.4	52.7

Table C.11
Same as Table 3 for masks in **17ESREGMAP01EXCERPT1**.

unit	$AP_{0.35}$	$AP_{0.50}$	AP	AP_S	AP_M	AP_L	$AR_{0.35}$	$AR_{0.50}$	AR	AR_S	AR_M	AR_L
bands	41.5	14.8	13.2	50.0	8.8	15.4	62.5	37.5	26.3	50.0	35.0	20.9
double ridges	31.4	29.7	13.4	0.4	17.3	0.0	48.5	42.4	20.9	10.0	23.2	0.0
ridge complexes	50.5	50.5	35.3	-100.0	0.0	70.0	50.0	50.0	35.0	-100.0	0.0	70.0
undiff. lineae	20.3	15.3	6.1	0.4	12.2	14.0	51.2	41.9	17.2	14.3	18.9	13.9
mean	35.9	27.6	17.0	16.9	9.6	24.8	53.1	42.9	24.8	24.7	19.3	26.2

Appendix E. LineaMapper on Ganymede

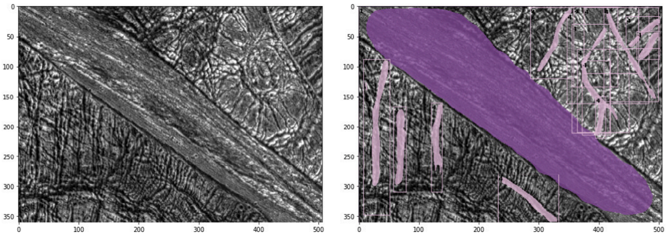

Fig. E.21. Performance of LineaMapper on Ganymede. Left: An image of the Galileo Regio at a resolution of 160 m/px (81 km displayed width), showing a bright band and dark terrain. Right: LineaMapper, which has only seen Galileo data of Europa during training, predicts a band, running from top left to bottom right, and undifferentiated lineae on both sides of the band. data source: https://photojournal.jpl.nasa.gov/catalog/PIA01616.

References

Aghaee, A., Shamsipour, P., Hood, S., Haugaard, R., 2021. A convolutional neural network for semi-automated lineament detection and vectorisation of remote sensing data using probabilistic clustering: A method and a challenge. Comput. Geosci. (ISSN: 00983004) 151 (March), 104724. http://dx.doi.org/10.1016/j.cageo.2021.104724.

Aydin, A., 2006. Failure modes of the lineaments on jupiter's moon, Europa: Implications for the evolution of its icy crust. J. Struct. Geol. (ISSN: 0191-8141) 28 (12), 2222–2236. http://dx.doi.org/10.1016/J.JSG.2006.08.003, URL https://ui.adsabs.harvard.edu/abs/2006JSG....28.2222A/abstract.

Azari, A.R., Biersteker, J.B., Dewey, R.M., Doran, G., Forsberg, E.J., Harris, C.D.K., Kerner, H.R., Skinner, K.A., Smith, A.W., Amini, R., Cambioni, S., Da Poian, V., Garton, T.M., Himes, M.D., Millholland, S., Ruhunusiri, S., Annex, A.M., Aye, K.-M., Argall, M.R., Cameron, M.E., Cao, X., Crary, F., Crichton, D.J., Cross, M., D'amore, M., De Wit, J., Francis, R., Helbert, J., Hood, D.R., Jackman, C.M., Lagain, A., Larson, R.E., Mai, C., Mandrake, L., Needham, A., Pankratius, V., Parr, J., Prockter, L.M., Pérez, F., Radebaugh, J., Theiling, B.P., Tiscareno, M., Vanderburg, A., Vandegriff, J., Hook, J.V., Varatharajan, I., Wagstaff, K., Waldmann, I., 2020. Integrating machine learning for planetary science: Perspectives for the next decade co-signers. arXiv 1–9, arXiv:2007.15129v1.

Barrett, A.M., Balme, M.R., Woods, M., Karachalios, S., Petrocelli, D., Joudrier, L., Sefton-Nash, E., 2022. NOAH-h, a deep-learning, terrain classification system for mars: Results for the ExoMars rover candidate landing sites. Icarus (ISSN: 10902643) 371 (114701), http://dx.doi.org/10.1016/j.icarus.2021.114701.

Beitzel, S.M., Jensen, E.C., Frieder, O., 2009. MAP. In: Encyclopedia of Database Systems. Springer, Boston, MA, Boston, MA, pp. 1691–1692. http://dx.doi.org/10.1007/978-0-387-39940-9_492, URL https://link.springer.com/referenceworkentry/10.1007/978-0-387-39940-9{_}492.

Belton, M.J.S., Klaasen, K.P., Clary, M.C., Anderson, J.L., Anger, C.D., Carr, M.H., Chapman, C.R., Davies, M.E., Greeley, R., Anderson, D., Bolef, L.K., Townsend, T.E., Greenberg, R., Iii, J.W.H., Neukum, G., Pilcher, C.B., Veverka, J., Gierasch, P.J., Fanale, F.P., Ingersoll, A.P., Masursky, H., Morrison, D., Pollack, J.B., 1992. The Galileo solid-state imaging experiment. Space Sci. Rev. 60, 413–455.

Bickel, V.T., Aaron, J., Manconi, A., Loew, S., Mall, U., 2020a. Impacts drive lunar rockfalls over billions of years. Nature Commun. (ISSN: 20411723) 11 (1), 1–7. http://dx.doi.org/10.1038/s41467-020-16653-3.

Bickel, V.T., Conway, S.J., Tesson, P.A., Manconi, A., Loew, S., Mall, U., 2020b. Deep learning-driven detection and mapping of rockfalls on mars. IEEE J. Sel. Top. Appl. Earth Obs. Remote Sens. (ISSN: 1939-1404) 13, 2831–2841. http://dx.doi.org/10.1109/JSTARS.2020.2991588.

Bickel, V.T., Lanaras, C., Manconi, A., Loew, S., Mall, U., 2019. Automated detection of lunar rockfalls using a convolutional neural network. IEEE Trans. Geosci. Remote Sens. 57 (6), http://dx.doi.org/10.1109/TGRS.2018.2885280, URL http://www.ieee.org/publications{_}standards/publications/rights/index.html.

Bickel, V.T., Loew, S., Aaron, J., Goedhart, N., 2022. A global perspective on lunar granular flows. Geophys. Res. Lett. (ISSN: 19448007) 49 (e2022GL098812), http://dx.doi.org/10.1029/2022GL098812.

Bland, M.T., Weller, L.A., Smith, E., Archinal, B.A., Benjamin, H., 2021. Improving the usability of Galileo and voyager images of jupiter ' s moon Europa. Earth Space Sci. 8 (12).

Blaney, D., Science, M., Team, E., 2022. The mapping imaging spectrometer for Europa (MISE): Instrument development status and expected science results. AAS/Div. Planet. Sci. Meet. Abstr. 54 (8), 521.05, URL https://ui.adsabs.harvard.edu/abs/2022DPS....5452105B/abstract.

Bradák, B., Kimura, J., Gomez, C., Kereszturi, Á., 2023. Separation of quasi-continuous and periodic components of lineament formation at the belus – phoenix - rhadamanthys linea "triangle" on Europa. Icarus (ISSN: 0019-1035) 391, 115367. http://dx.doi.org/10.1016/J.ICARUS.2022.115367, URL https://linkinghub.elsevier.com/retrieve/pii/S0019103522004596.

Collins, G.C., Patterson, G.W., Detelich, C.E., Prockter, L.M., Kattenhorn, S.A., Cooper, C.M., Rhoden, A.R., Cutler, B.B., Oldrid, S.R., Perkins, R.P., Rezza, C.A., 2022. Episodic plate tectonics on Europa: Evidence for widespread patches of mobile-lid behavior in the antijovian hemisphere. J. Geophys. Res.: Planets (ISSN: 21699100) 127 (11), http://dx.doi.org/10.1029/2022JE007492.

Craft, K.L., Patterson, G.W., Lowell, R.P., Germanovich, L., 2016. Fracturing and flow: Investigations on the formation of shallow water sills on Europa. Icarus (ISSN: 0019-1035) 274, 297–313. http://dx.doi.org/10.1016/J.ICARUS.2016.01.023.

Crawford, G.D., Stevenson, D.J., 1988. Gas-driven water volcanism and the resurfacing of Europa. Icarus (ISSN: 0019-1035) 73 (1), 66–79. http://dx.doi.org/10.1016/0019-1035(88)90085-1.

Culberg, R., Schroeder, D.M., Steinbrügge, G., 2022. Double ridge formation over shallow water sills on jupiter's moon Europa. Nature Commun. (ISSN: 2041-1723) 13 (1), 2007. http://dx.doi.org/10.1038/s41467-022-29458-3, URL https://www.nature.com/articles/s41467-022-29458-3,

Dameron, A.C., Burr, D.M., 2018. Europan double ridge morphometry as a test of formation models. Icarus (ISSN: 0019-1035) 305, 225–249. http://dx.doi.org/10.1016/J.ICARUS.2017.12.009.

Del Prete, R., Renga, A., 2022. A novel visual-based terrain relative navigation system for planetary applications based on mask R-CNN and projective invariants. Aerotecnica Missili Spazio (ISSN: 2524-6968) 101, 335–349. http://dx.doi.org/10.1007/S42496-022-00139-0, URL https://link.springer.com/article/10.1007/s42496-022-00139-0,

Deng, J., Dong, W., Socher, R., Li, L.-J., Li, K., Fei-Fei, L., 2009. Imagenet: A large-scale hierarchical image database. In: 2009 IEEE Conference on Computer Vision and Pattern Recognition. Ieee, pp. 248–255.

Doggett, T., Greeley, R., Figueredo, P., 2009. Geologic stratigraphy and evolution of Europa's surface. In: Europa. pp. 137–159.

Dombard, A.J., Patterson, G.W., Lederer, A.P., Prockter, L.M., 2013. Flanking fractures and the formation of double ridges on Europa. Icarus (ISSN: 0019-1035) 223 (1), 74–81. http://dx.doi.org/10.1016/J.ICARUS.2012.11.021.

Duda, R.O., Hart, P.E., 1972. Use of the hough transformation to detect lines and curves in pictures. Commun. ACM (ISSN: 15577317) 15 (1), 11–15. http://dx.doi.org/10.1145/361237.361242.

Figueredo, P.H., Greeley, R., 2000. Geologic mapping of the northern leading hemisphere of Europa from Galileo solid-state imaging data. J. Geophys. Res.: Planets (ISSN: 01480227) 105 (E9), 629–651. http://dx.doi.org/10.1029/1999JE001107.

Figueredo, P.H., Greeley, R., 2004. Resurfacing history of Europa from pole-to-pole geological mapping. Icarus 167 (2), 287–312. http://dx.doi.org/10.1016/J.ICARUS.2003.09.016.

Ford, J.P., Blom, R.G., Crisp, J.A., Elachi, C., Farr, T.G., Saunders, R.S., Theilig, E.E., Wall, S.D., Yewell, S.B., 1989. Spaceborne radar observations: A guide for magellan radar-image analysis. JPL Publ. 89–41.

Ford, J.P., Plaut, J.J., Weitz, C.M., Farr, T.G., Senske, D.A., Stofan, E.R., Michaels, G., Parker, T.J., Fulton, D., 1993. Guide to magellan image interpretation. JPL Publ. 93–24, 1–18.

Gaidos, E.J., Nimmo, F., 2000. Tectonics and water on Europa. Nature 405 (6787).

Gan, Y., You, S., Luo, Z., Liu, K., Zhang, T., Du, L., 2020. Object detection in remote sensing images with mask R-CNN. J. Phys. Conf. Ser. (ISSN: 17426596) 1673 (012040), http://dx.doi.org/10.1088/1742-6596/1673/1/012040.

Geissler, P.E., Greenberg, R., Hoppa, G., Helfenstein, P., McEwen, A., Pappalardo, R., Tufts, R., Ockert-Bell, M., Sullivan, R., Greeley, R., Belton, M.J., Denk, T., Clark, B., Burns, J., Veverka, J., 1998a. Evidence for non-synchronous rotation of Europa. Nature (ISSN: 1476-4687) 391 (6665), 368–370. http://dx.doi.org/10.1038/34869, URL https://www.nature.com/articles/34869.

Geissler, P.E., Greenberg, R., Hoppa, G., McEwen, A., Tufts, R., Phillips, C., Clark, B., Ockert-Bell, M., Helfenstein, P., Burns, J., Veverka, J., Sullivan, R., Greeley, R., Pappalardo, R.T., Head, J.W., Belton, M.J., Denk, T., 1998b. Evolution of lineaments on Europa: Clues from Galileo multispectral imaging observations. Icarus (ISSN: 0019-1035) 135 (1), 107–126. http://dx.doi.org/10.1006/ICAR.1998.5980.

Gonzalez, R.C., Wintz, P., 1977. Digital Image Processing.

Goodfellow, I., Bengio, Y., Courville, A., 2016. Deep Learning. MIT Press.

Greeley, R., Figueredo, P.H., Williams, D.A., Chuang, F.C., Klemaszewski, J.E., Kadel, S.D., Prockter, L.M., Pappalardo, R.T., Head, J.W., Collins, G.C., Spaun, N.A., Sullivan, R.J., Moore, J.M., Senske, D.A., Tufts, B.R., Johnson, T.V., Belton, M.J., Tanaka, K.L., 2000. Geologic mapping of Europa. J. Geophys. Res. E: Planets 105 (E9), 22559–22578. http://dx.doi.org/10.1029/1999JE001173.

Greeley, R., Sullivan, R., Klemaszewski, J., Homan, K., Head, J.W., Pappalardo, R.T., Veverka, J., Clark, B.E., Johnson, T.V., Klaasen, K.P., Belton, M., Moore, J., Asphaug, E., Carr, M.H., Neukum, G., Denk, T., Chapman, C.R., Pilcher, C.B., Geissler, P.E., Greenberg, R., Tufts, R., 1998. Europa: Initial Galileo geological observations. Icarus (ISSN: 0019-1035) 135 (1), 4–24. http://dx.doi.org/10.1006/ICAR.1998.5969.

Greenberg, R., Geissler, P., 2002. Europa's dynamic icy crust. Meteorit. Planet. Sci. (ISSN: 10869379) 37 (12), 1685–1710. http://dx.doi.org/10.1111/J.1945-5100.2002.TB01158.X.

Greenberg, R., Geissler, P., Hoppa, G., Tufts, B.R., Durda, D.D., Pappalardo, R., Head, J.W., Greeley, R., Sullivan, R., Carr, M.H., 1998a. Tectonic processes on Europa: Tidal stresses, mechanical response, and visible features. Icarus (ISSN: 0019-1035) 135 (1), 64–78. http://dx.doi.org/10.1006/ICAR.1998.5986.

Greenberg, R., Geissler, P., Hoppa, G., Tufts, B.R., Durda, D.D., Pappalardo, R., Head, J.W., Greeley, R., Sullivan, R., Carr, M.H., 1998b. Tectonic processes on Europa: Tidal stresses, mechanical response, and visible features. Icarus (ISSN: 0019-1035) 135 (1), 64–78. http://dx.doi.org/10.1006/ICAR.1998.5986.

Greenberg, R., Hoppa, G.V., Tufts, B.R., Geissler, P., Riley, J., Kadel, S., 1999. Chaos on Europa. Icarus (ISSN: 00191035) 141 (2), 263–286. http://dx.doi.org/10.1006/icar.1999.6187.

Groenleer, J.M., Kattenhorn, S.A., 2008. Cycloid crack sequences on Europa: Relationship to stress history and constraints on growth mechanics based on cusp angles. Icarus (ISSN: 0019-1035) 193 (1), 158–181. http://dx.doi.org/10.1016/J.ICARUS.2007.08.032.

Han, L., Melosh, H.J., 2010. Origin of Europa's ridges by incremental ice-wedging. Am. Geophys. Union, Fall Meet. 2010, Abstract #P33B-1577 https://ui.adsabs.harvard.edu/abs/2010AGUFM.P33B1577H/abstract, http://adsabs.harvard.edu/abs/2010AGUFM.P33B1577H.

Han, L., Showman, A.P., 2008. Implications of shear heating and fracture zones for ridge formation on Europa. Geophys. Res. Lett. (ISSN: 1944-8007) 35 (3), 3202. http://dx.doi.org/10.1029/2007GL031957, https://onlinelibrary.wiley.com/doi/full/10.1029/2007GL031957, https://onlinelibrary.wiley.com/doi/abs/10.1029/2007GL031957, https://agupubs.onlinelibrary.wiley.com/doi/10.1029/2007GL031957.

Harada, Y., Kurita, K., 2006. The dependence of surface tidal stress on the internal structure of Europa: The possibility of cracking of the icy shell. Planet. Space Sci. (ISSN: 0032-0633) 54 (2), 170–180. http://dx.doi.org/10.1016/J.PSS.2005.12.001.

He, K., Gkioxari, G., Dollár, P., Girshick, R., 2018. Mask R-CNN. URL https://github.com/.

He, K., Zhang, X., Ren, S., Sun, J., 2016. Deep residual learning for image recognition. In: 2016 IEEE Conference on Computer Vision and Pattern Recognition. (CVPR), IEEE Computer Society, (ISSN: 10636919) ISBN: 9781467388504, pp. 770–778. http://dx.doi.org/10.1109/CVPR.2016.90, arXiv:1512.03385.

Head, J.W., Pappalardo, R.T., Sullivan, R., 1999. Europa: Morphological characteristics of ridges and triple bands from Galileo data (E4 and E6) and assessment of a linear diapirism model. J. Geophys. Res. E: Planets (ISSN: 01480227) 104 (E10), 24223–24236. http://dx.doi.org/10.1029/1998JE001011.

Head, J.W., Sherman, N.D., Pappalardo, R.T., Greeley, R., Sullivan, R., Senske, D., Mcewen, A., 1998. Geologic history of the E4 region of Europa: Implications for ridge formation, cryovolcanism, and chaos formation. In: Lunar and Planetary Science XXIX. p. 1412.

Hoppa, G.V., Tufts, B.R., Greenberg, R., Geissler, P.E., 1999. Formation of cycloidal features on Europa. Science (ISSN: 0036-8075) 285 (5435), 1899–1902. http://dx.doi.org/10.1126/SCIENCE.285.5435.1899, URL https://pubmed.ncbi.nlm.nih.gov/10489365/.

Hurford, T.A., Sarid, A.R., Greenberg, R., 2007. Cycloidal cracks on Europa: Improved modeling and non-synchronous rotation implications. Icarus (ISSN: 0019-1035) 186 (1), 218–233. http://dx.doi.org/10.1016/J.ICARUS.2006.08.026.

Hurford, T.A., Sarid, A.R., Greenberg, R., Bills, B.G., 2009. The influence of obliquity on Europan cycloid formation. Icarus (ISSN: 0019-1035) 202 (1), 197–215. http://dx.doi.org/10.1016/J.ICARUS.2009.02.036.

Johnston, S.A., Montési, L.G., 2014. Formation of ridges on Europa above crystallizing water bodies inside the ice shell. Icarus (ISSN: 0019-1035) 237, 190–201. http://dx.doi.org/10.1016/J.ICARUS.2014.04.026.

Jung, A.B., Wada, K., Crall, J., Tanaka, S., Graving, J., Reinders, C., Yadav, S., Banerjee, J., Vecsei, G., Kraft, A., Rui, Z., Borovec, J., Vallentin, C., Zhydenko, S., Pfeiffer, K., Cook, B., Fernández, I., De Rainville, F.-M., Weng, C.-H., Ayala-Acevedo, A., Meudec, R., Laporte, M., et al., 2020. Imgaug. https://github.com/aleju/imgaug.

Kadel, S.D., Fagents, S.A., Greeley, R., Galileo SSI Team, 1998. Trough-bounding ridge pairs on Europa – considerations for an endogenic model of formation. In: 29th Lunar Planetary Science Conference. p. 1078.

Kalousová, K., Souček, O., Tobie, G., Choblet, G., Čadek, O., 2016. Water generation and transport below Europa's strike-slip faults. J. Geophys. Res.: Planets (ISSN: 2169-9100) 121 (12), 2444–2462. http://dx.doi.org/10.1002/2016JE005188, https://onlinelibrary.wiley.com/doi/full/10.1002/2016JE005188, https://onlinelibrary.wiley.com/doi/abs/10.1002/2016JE005188, https://agupubs.onlinelibrary.wiley.com/doi/10.1002/2016JE005188,

Kattenhorn, S.A., 2002. Nonsynchronous rotation evidence and fracture history in the bright plains region, Europa. Icarus (ISSN: 00191035) 157 (2), 490–506.

Kattenhorn, S.A., Hurford, T., 2009. Tectonics of Europa. In: Europa. pp. 199–236. http://dx.doi.org/10.2307/j.ctt1xp3wdw.15.

Kattenhorn, S.A., Prockter, L.M., 2014. Evidence for subduction in the ice shell of Europa. Nat. Geosci. 7 (10), 762–767. http://dx.doi.org/10.1038/NGEO2245.

Kiryati, N., Eldar, Y., Bruckstein, A.M., 1991. A probabilistic hough transform. Pattern Recognit. (ISSN: 0031-3203) 24 (4), 303–316. http://dx.doi.org/10.1016/0031-3203(91)90073-E.

Kisantal, M., Wojna, Z., Murawski, J., Naruniec, J., Cho, K., 2019. Augmentation for small object detection. In: 9th International Conference on Advances in Computing and Information Technology. pp. 119–133. http://dx.doi.org/10.5121/csit.2019.91713.

Leonard, E.J., Pappalardo, R.T., Yin, A., 2018. Analysis of very-high-resolution Galileo images and implications for resurfacing mechanisms on Europa. Icarus (ISSN: 10902643) 312, 100–120. http://dx.doi.org/10.1016/j.icarus.2018.04.016.

Leonard, E.J., Senske, D.A., Patthoff, D.A., 2019. Global and regional scale geologic mapping of Europa. EPSC-DPS2019-57-1 13.

Lucchitta, B.K., Soderblom, L.A., 1982. Satellites of jupiter. Univ. Arizona Press 521 (4), 17–21.

Mais, L., Hirsch, P., Kainmueller, D., 2020. PatchPerPix for instance segmentation. In: Vedaldi, A., Bischof, H., Brox, T., Frahm, J.-M. (Eds.), Computer Vision – ECCV 2020, Vol. 12370 LNCS. Springer International Publishing, Cham, (ISSN: 16113349) ISBN: 978-3-030-58595-2, pp. 288–304. http://dx.doi.org/10.1007/978-3-030-58595-2_18/FIGURES/4, URL https://link.springer.com/chapter/10.1007/978-3-030-58595-2_18.

Manga, M., Sinton, A., 2004. Formation of bands and ridges on Europa by cyclic deformation: Insights from analogue wax experiments. J. Geophys. Res. E: Planets 109 (E09001), http://dx.doi.org/10.1029/2004JE002249.

Marcel, S., Rodriguez, Y., 2010. Torchvision the machine-vision package of torch. In: MM'10 - Proceedings of the ACM Multimedia 2010 International Conference. ISBN: 9781605589336, pp. 1485–1488. http://dx.doi.org/10.1145/1873951.1874254, URL https://dl.acm.org/doi/10.1145/1873951.1874254.

Marshall, S.T., Kattenhorn, S.A., 2005. A revised model for cycloid growth mechanics on Europa: Evidence from surface morphologies and geometries. Icarus (ISSN: 0019-1035) 177 (2), 341–366. http://dx.doi.org/10.1016/J.ICARUS.2005.02.022.

Melosh, H.J., Turtle, E.P., 2004. Ridges on Europa: Origin by incremental ice-wedging. Lunar Planet. Inst. Sci. Conf. Abstr. 35, 2029, URL http://adsabs.harvard.edu/abs/2004LPI....35.2029M.

Nimmo, F., Gaidos, E., 2002. Strike-slip motion and double ridge formation on Europa. J. Geophys. Res. E: Planets (ISSN: 01480227) 107 (4), http://dx.doi.org/10.1029/2000je001476.

Nixon, C.A., Yahn, Z., Duncan, E., Neidel, I., Mills, A.C., Seignovert, B., Larsen, A., Gansler, K., Liles, C., Walker, C.C., Trent, D.M., Santerre, J., 2023. Feature extraction and classification from planetary science datasets enabled by machine learning. In: 2023 IEEE Aerospace Conference. IEEE, ISBN: 978-1-6654-9032-0, pp. 1–16. http://dx.doi.org/10.1109/AERO55745.2023.10115556, URL https://ieeexplore.ieee.org/document/10115556/.

Noviello, J.L., Torrano, Z.A., Rhoden, A.R., Singer, K.N., 2019. Mapping Europa's microfeatures in regional mosaics: New constraints on formation models. Icarus (ISSN: 0019-1035) 329, 101–123. http://dx.doi.org/10.1016/J.ICARUS.2019.02.038.

Pappalardo, R.T., Belton, M.J., Breneman, H.H., Carr, M.H., Chapman, C.R., Collins, G.C., Denk, T., Fagents, S., Geissler, P.E., Giese, B., Greeley, R., Greenberg, R., Head, J.W., Helfenstein, P., Hoppa, G., Kadel, S.D., Klaasen, K.P., Klemaszewski, J.E., Magee, K., McEwen, A.S., Moore, J.M., Moore, W.B., Neukum, G., Phillips, C.B., Prockter, L.M., Schubert, G., Senske, D.A., Sullivan, R.J., Tufts, B.R., Turtle, E.P., Wagner, R., Williams, K.K., 1999. Does Europa have a subsurface ocean? Evaluation of the geological evidence. J. Geophys. Res.: Planets (ISSN: 01480227) 104 (E10), 24015–24055. http://dx.doi.org/10.1029/1998JE000628.

Pappalardo, R., Coon, M.D., 1996. A sea ice analog for the surface of Europa. Lunar Planet. Sci. 27, 997–998,

Pappalardo, R., Patthoff, D., Li, J.B., Ayton, B., Dubois, D., Dubois Cycloidal, D., Lineaments, W., Pappalardo, R.T., Patthoff, D.A., Ayton, B.J., Dubois, D., 2016. Cycloidal and wavy lineaments on Europa from diurnal, obliquity, and nonsynchronous rotation stresses in a visco-elastic ice shell. In: LPSC 2016 - 47th Lunar and Planetary Science Conference, Vol. hal-012744. p. 2712, https://hal.science/hal-01274499, https://hal.science/hal-01274499/document.

Paszke, A., Gross, S., Massa, F., Lerer, A., Bradbury Google, J., Chanan, G., Killeen, T., Lin, Z., Gimelshein, N., Antiga, L., Desmaison, A., Xamla, A.K., Yang, E., Devito, Z., Raison Nabla, M., Tejani, A., Chilamkurthy, S., Ai, Q., Steiner, B., Facebook, L.F., Facebook, J.B., Chintala, S., 2019. Pytorch: An imperative style, high-performance deep learning library. In: 33rd Conference on Neural Information Processing Systems. pp. 8026–8037.

Patterson, G.W., Head, J.W., 2010. Segmented lineaments on Europa: Implications for the formation of ridge complexes and bright bands. Icarus (ISSN: 0019-1035) 205 (2), 528–539. http://dx.doi.org/10.1016/J.ICARUS.2009.07.045.

Patterson, G.W., Head, J.W., Pappalardo, R.T., 2006. Plate motion on Europa and nonrigid behavior of the icy lithosphere: The Castalia Macula region. J. Struct. Geol. (ISSN: 0191-8141) 28 (12), 2237–2258. http://dx.doi.org/10.1016/J.JSG.2006.03.032.

Poinelli, M., Larour, E., Castillo-Rogez, J., Vermeersen, B., 2019. Crevasse propagation on brittle ice: Application to cycloids on Europa. Geophys. Res. Lett. (ISSN: 1944-8007) 46 (21), 11756–11763. http://dx.doi.org/10.1029/2019GL084033, https://onlinelibrary.wiley.com/doi/full/10.1029/2019GL084033, https://onlinelibrary.wiley.com/doi/abs/10.1029/2019GL084033, https://agupubs.onlinelibrary.wiley.com/doi/10.1029/2019GL084033.

Prockter, L.M., Patterson, G.W., 2009. Morphology and evolution of Europa's ridges and bands. In: Europa. pp. 237–258. http://dx.doi.org/10.2307/j.ctt1xp3wdw.16.

QGIS Development Team, 2022. QGIS Geographic Information System. QGIS Association, URL https://www.qgis.org.

Radon, J., 1917. Über die bestimmung von funktionen durch ihre integralwerte längs gewisser mannigfaltigkeiten. Ber. Sächsische AKadamie Wissenschaften 69, 262–267. http://dx.doi.org/10.1090/psapm/027/692055.

Rhoden, A.R., Hurford, T.A., 2013. Lineament azimuths on Europa: Implications for obliquity and non-synchronous rotation. Icarus (ISSN: 0019-1035) 226 (1), 841–859. http://dx.doi.org/10.1016/J.ICARUS.2013.06.029.

Rhoden, A.R., Hurford, T.A., Roth, L., Retherford, K., 2015. Linking Europa's plume activity to tides, tectonics, and liquid water. Icarus (ISSN: 0019-1035) 253, 169–178. http://dx.doi.org/10.1016/J.ICARUS.2015.02.023, arXiv:1502.06854.

Rhoden, A.R., Militzer, B., Huff, E.M., Hurford, T.A., Manga, M., Richards, M.A., 2010. Constraints on Europa's rotational dynamics from modeling of tidally-driven fractures. Icarus (ISSN: 00191035) 210 (2), 770–784. http://dx.doi.org/10.1016/j.icarus.2010.07.018.

Rhoden, A.R., Mohr, K.J., Hurford, T.A., Henning, W., Sajous, S., Patthoff, D.A., Dubois, D., 2021. Obliquity, precession, and fracture mechanics: Implications of Europa's global cycloid population. J. Geophys. Res.: Planets (ISSN: 2169-9100) 126 (3), http://dx.doi.org/10.1029/2020JE006710, e2020JE006710, https://onlinelibrary.wiley.com/doi/full/10.1029/2020JE006710, https://onlinelibrary.wiley.com/doi/abs/10.1029/2020JE006710, https://agupubs.onlinelibrary.wiley.com/doi/10.1029/2020JE006710.

Robbins, H., Monro, S., 1951. A stochastic approximation method. 22, (3), (ISSN: 0003-4851) pp. 400–407. http://dx.doi.org/10.1214/AOMS/1177729586, https://projecteuclid.org/journals/annals-of-mathematical-statistics/volume-22/issue-3/A-Stochastic-Approximation-Method/10.1214/aoms/1177729586.full, https://projecteuclid.org/journals/annals-of-mathematical-statistics/volume-22/issue-3/A-Stochastic-Approximation-Method/10.1214/aoms/1177729586.short.

Ruzicka, B.-K., Schröter, M., Pack, A., Boehnhardt, H., 2021. Detecting and analysing geomorphological structures in images of comet 67P/Churyumov-Gerasimenko using Fourier transform. 11, (March), pp. 1–11. http://dx.doi.org/10.1093/mnras/stab618, URL http://arxiv.org/abs/2103.00970%0A.

Sarid, A.R., Greenberg, R., Hoppa, G.V., Brown, D.M., Geissler, P., 2005. Crack azimuths on Europa: The G1 lineament sequence revisited. Icarus (ISSN: 00191035) 173 (2), 469–479. http://dx.doi.org/10.1016/j.icarus.2004.08.011.

Sarid, A.R., Greenberg, R., Hoppa, G.V., Geissler, P., Preblich, B., 2004. Crack azimuths on Europa: Time sequence in the southern leading face. Icarus (ISSN: 00191035) 168 (1), 144–157. http://dx.doi.org/10.1016/j.icarus.2003.11.021.

Sarid, A.R., Greenberg, R., Hurford, T.A., 2006. Crack azimuths on Europa: Sequencing of the northern leading hemisphere. J. Geophys. Res.: Planets (ISSN: 01480227) 111 (8), http://dx.doi.org/10.1029/2005JE002524.

Sullivan, R., Greeley, R., Homan, K., Klemaszewski, J., Belton, M.J., Carr, M.H., Chapman, C.R., Tufts, R., Head, J.W., Pappalardo, R., Moore, J., Thomas, P., 1998. Episodic plate separation and fracture infill on the surface of Europa. Nature 391 (6665), 371–373. http://dx.doi.org/10.1038/34874.

Tufts, B.R., Greenberg, R., Hoppa, G., Geissler, P., 2000. Lithospheric dilation on Europa. Icarus (ISSN: 0019-1035) 146 (1), 75–97. http://dx.doi.org/10.1006/ICAR.2000.6369.

Turtle, E.P., Mcewen, A.S., Patterson, G.W., Ernst, C.M., Elder, C.M., Tucker, O.J., Torres, I., Thomas, N., Sutton, S., Stickle, A., Soderblom, J.M., Slack, K.A., Seifert, H., Robbins, G., Quick, L.C., Prockter, L., Pommerol, A., Phillips, C.B., Nimmo, F., Niewola, J., Mlinar, A.C.B., Mills, M., Meyer, H., Mcdermott, J., Kutsop, N., Kirk, R.L., Hurford, T.A., Humm, D., Hayes, A.G., Hawkins, S.E., Haslebacher, C., Hansen, C.J., Fletcher, L., Demajistre, R., Detelich, C., Daubar, I.J., Corlies, P., Collins, G.C., Bland, M., 2023. The Europa imaging system (eis) flight instruments in spacecraft and environmental testing for Europa clipper. In: 54th Lunar and Planetary Science Conference. p. 5232.

Turtle, E.P., Melosh, H.J., Phillips, C.B., 1998. Europan ridges: Tectonic response to dike intrusion. Eos Trans. AGU 79 (17), S202.

U.S. Geological Survey, 2002. Controlled photomosaic map of Europa, Je 15M CMN. URL https://pubs.usgs.gov/imap/i2757/.

Wang, H., Raj, B., 2017. On the origin of deep learning. arXiv.

Zhang, W., Liljedahl, A.K., Kanevskiy, M., Epstein, H.E., Jones, B.M., Jorgenson, M.T., Kent, K., 2020. Transferability of the deep learning mask R-CNN model for automated mapping of ice-wedge polygons in high-resolution satellite and UAV images. Remote Sens. (ISSN: 2072-4292) 12 (7), 1085. http://dx.doi.org/10.3390/RS12071085, https://www.mdpi.com/2072-4292/12/7/1085/htm, https://www.mdpi.com/2072-4292/12/7/1085.